5-2024

SYNTHESIS OF GOLD NANOPARTICLES VIA PULSED LIQUID ABLATION FOR USE IN THE PHOTODYNAMIC THERAPY OF BACTERIA

Justice ben Yosef

SYNTHESIS OF GOLD NANOPARTICLES VIA PULSED LIQUID ABLATION FOR USE IN THE PHOTODYNAMIC THERAPY OF BACTERIA

A Thesis submitted in partial fulfillment
of the requirements for the degree
Master of Science

Department of Chemistry
Western Kentucky University
Bowling Green, Kentucky

By
Justice ben Yosef

May, 2024

SYNTHESIS OF GOLD NANOPARTICLES VIA PULSED LIQUID ABLATION FOR USE IN THE PHOTODYNAMIC THERAPY OF BACTERIA

Justice ben Yosef

Date Recommended 4/11/2024

DocuSigned by:
ali oguz er
F0511F8EF47B4C8...
Chair

DocuSigned by:
Lawrence Hill
F76E7D325CDF411...
Committee Member

DocuSigned by:
Matthew Mc
060FA5FC6F1241C...
Committee Member

Committee Member

DocuSigned by:
Jennifer Hammonds
EBE3858E068F42D...
Interim Director of the Graduate School

ABSTRACT

SYNTHESIS OF GOLD NANOPARTICLES VIA PULSED LIQUID ABLATION FOR USE IN THE PHOTODYNAMIC THERAPY OF BACTERIA

With the ever-increasing threat of antibiotic resistant bacteria, alternative treatment methods have been developed including photodynamic therapy (PDT). Within the PDT process, photosensitizers are used to generate reactive oxygen species (ROS) and facilitate the cell termination process. This work lays the conceptual foundation for the functionalization of the photosensitizer methylene blue (MB) with gold nanoparticles (AuNPs) and INF-55 as a potential inhibitor of the AcrAB-TolC efflux pump to enhance the effectivity of the PDT process.

AuNPs were synthesized using pulsed laser ablation in an aqueous citrate solution. Both nanosecond and picosecond pulse durations, as well as both 532 nm and 1064 nm wavelengths at various powers and frequencies were tested to determine the effect of laser parameters on particle synthesis. The nanosecond, 532 nm, 2.0 W laser parameters were determined to produce the most viable AuNPs for application in PDT with an average Feret diameter of 7.46 ± 3.28 nm. After synthesis, the AuNPs were characterized using transmission electron microscopy imaging, UV-Visible spectroscopy, fluorescence spectroscopy, and Fourier transform infrared (FTIR) Spectroscopy.

After synthesis and characterization of the AuNPs, the ROS generated in solution was measured by monitoring the photobleaching of 9,10-Anthracenediyl-bis(methylene)dimalonic Acid (ABMDMA). Molecular docking calculations were conducted to determine the viability of INF-55 as a competitive inhibitor for the AcrB subunit. The most probable binding mode for INF-55 had a binding affinity of –9.1 kcal/mol while the most probable binding mode for MB had a binding affinity of –7.2 kcal/mol.

Additionally, AuNPs were used in combination with MB in-vitro on the Gram-negative bacteria *Escherichia coli* (*E. coli*) to determine the effect of AuNPs on cell termination. When AuNPs were used with MB, a 99.98 - 99.99 % decrease in the bacteria concentration was observed as compared to a 97.51 % decrease with MB alone.

I dedicate this thesis to my parents and sister for their endless support throughout my academic career.

ACKNOWLEDGMENTS

First, I would like to thank Dr. Ali Er for his continued support and mentorship throughout both my undergraduate and graduate research experience as well as his willingness to take me on as a research student from the chemistry department. I would also like to thank the entirety of the chemistry department, specifically Dr. Kevin Williams, Dr. Matthew Nee, and Dr. Lawrence Hill for all of their support and for making the JUMP program possible. I would like to thank Dr. John Andersland from the biology department as well for being continuously helpful and a tremendous resource when it came to anything and everything microscopy related.

I would like to acknowledge my lab mate Yaran Allamyradov for his boundless help, reassurance, and late-night experimental contributions. I would also like to thank the graduate student before me, Somon Hakimov, for teaching me everything he learned and giving me a strong experimental foundation to build upon. I would also like to thank Salizhan, Zirkulloh, Inomjon, Chazz, Carli, and Hadley, from the laser lab, as well as Brian, Zach, Chris, Hannah, Sammuel, Emmanuel, Jihye, and the rest of my chemistry cohort for their continuous positivity, support, and friendship.

Finally, I would like to thank my family for their endless sacrifices to help me achieve my goals. Without their foundation, I would not be where I am today. And, most importantly, I would like to thank God for giving me strength and endless opportunities and for always being the set of footprints in the sand next to me throughout my entire life.

TABLE OF CONTENTS

LIST OF TABLES

LIST OF FIGURES

CHAPTER 1

INTRODUCTION

1.1 Significance of Antibiotic Resistance

When looking back at scientific discoveries throughout history, among the most notable scientific advancements in medicine occurred in the early to mid-20th century with the discovery, isolation, and production of penicillin as an antibiotic compound. In 1928, Alexander Fleming discovered the antibacterial effects of *P. notatum*, leading Ernst Chain and Howard Florey to isolate penicillin in 1939.[1] Due to the significance of their research, Fleming, Chain, and Florey received the Nobel Prize in Medicine and Physiology in 1945.[1,2] Since the discovery of penicillin, antibiotics have become a significant area of scientific research due to their ability to combat previously untreatable bacterial infections.[3]

Over the past few decades, bacterial infections have re-emerged as a significant threat to public health due to the overprescription and overuse of antibiotics.[4,5] It is estimated that approximately 30% of the antibiotics prescribed in the clinical setting are unnecessary for the intended application.[4,5] When combined with the recent void in the development of novel antibiotics, alternative treatment methods have become a significant topic of research within multiple scientific disciplines to combat multidrug resistant bacteria (MDR).[6–10]

One of the most frequently cited statistics related to antibiotic resistance is the Center of Disease Control's (CDC) Antibiotic Threat in the United States reports. According to these documents, it is estimated that more than 2.8 million antibiotic resistant bacterial infections were reported in 2019, leading to more than 35,000 deaths in the United States alone.[11] When compared

to the 2 million infections resulting in 23,000 deaths reported in 2013, cases of antibiotic resistance have increased by 40% over the span of 6 years.[12] Additionally, the number of deaths from such infections has increased by 52% in 6 years despite preventative measures.[11,12] As portrayed by the statistical data, multidrug resistant bacteria are a current, major threat to public health.

Advancements in technology and scientific understanding have allowed for the development of enhanced bacterial treatment methods to combat MDR bacteria including combination therapies, engineered bacteriophages, photothermal therapy (PTT), and photodynamic therapy (PDT).[13–16] Among these new methods, photodynamic therapy has become a leading alternative due to its relative simplicity, versatility, and clinical potential.[13,14]

1.2 Photodynamic Therapy Background

Photodynamic therapy is a treatment method that utilizes photosensitive chemical compounds, called photosensitizers, to combat bacterial infections, cancerous tumors, abnormal skin/eye conditions, etc.[13–15] Understanding the chemical mechanism behind PDT has been crucial for its advancement and refinement. It has been well demonstrated in the literature that photosensitizers are chemical compounds that transition from a ground singlet state to an excited singlet state upon irradiation with a particular wavelength of light.[15] When in this excited singlet state, the photosensitizer can either relax back to a lower energy state via fluorescence or vibrational relaxation, or it can transition to an excited triplet state via intersystem crossing. Once in the excited triplet state, the photosensitizer can again, either relax back to a lower energy singlet state via phosphorescence, or it can react with molecular oxygen in one of two types of reactions to generate reactive oxygen species (ROS).[15]

Type I reactions occur when the excited triplet state photosensitizer interacts with a molecular substrate to generate radical species.[15] These radical species subsequently react with molecular oxygen to form oxygenated products such as hydrogen peroxide (H_2O_2), hydroxy radicals ($OH^{\bullet}$), and superoxide anions ($O_2^{-\bullet}$). Type II reactions, conversely, occur when the activated photosensitizer reacts directly with molecular oxygen to form singlet oxygen ($^1O_2$). Each of these reactive oxygen species can then react with cellular substrates, making them highly toxic to various cellular components such as the cell membrane, resulting in cellular death via apoptosis or necrosis.[13,15] This photosensitizer mechanism is summarized and depicted in Figure 1.

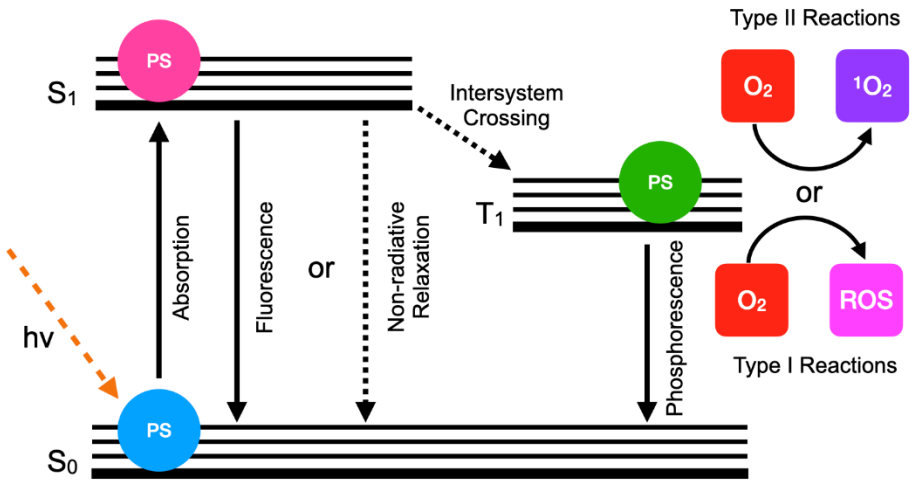

Figure 1: Schematic of the mechanism for singlet oxygen ($^1O_2$) and reactive oxygen species (ROS) generation from a photosensitizer (PS). The photosensitizer begins in a ground singlet (S_0) state. When irradiated with a particular wavelength of light (hv) it enters an excited singlet state (S_1). After intersystem crossing, it enters an excited triplet state (T_1) where it can react with molecular oxygen (O_2) to produce singlet oxygen and ROS.

Once generated in-situ, the relatively short half-life of ROS in biological tissues allows for site directed treatments as cells within the relative proximity of the photosensitizer will be

impacted by the generation of ROS.[14] By introducing photosensitizing agents directly at the treatment site and irradiating the area, cell death can be induced either directly or indirectly. Indirect cell death can occur by damaging related vasculature or by activating the immune response. Direct cell death, on the other hand, can occur through the destruction or disruption of various cellular components including the membrane, cellular proteins, DNA, or ribosomes.[16] Due to its localizability, PDT has become a recent topic of study with the intent to improve the process for further application in clinical treatments.[13,15]

When studied independently, PDT has limitations which restrict its effectiveness including low concentrations of produced ROS, the introduction and localization of the photosensitizing agents, and light penetration within biological tissues.[14] Various methods to overcome these limitations have been proposed including the introduction of nanomaterials.[17–23]

The photosensitizer used in this work is methylene blue (MB). MB belongs to a class of compounds known as phenothiaziniums which are heterocyclic compounds that contain nitrogen and sulfur.[24] Since its synthesis in 1856 for use in the textile industry, MB has been used for cellular staining, for the treatment of malaria, as a redox indicator, and as a photosensitizer in PDT as it has a peak absorbance between 600 - 668 nm.[25] When used independently, MB has been proven to be effective in the photodeactivation of bacteria in multiple cases for both gram-negative and gram-positive bacteria.[26–28] However, as previously mentioned, limitations such as low singlet oxygen yields are still prevalent and have sparked new research which aims to overcome the restrictions of the PDT process and further improve its effectivity.

1.3 Application and Synthesis of Gold Nanoparticles

The introduction and use of nanomaterials for the treatment of bacterial infections has recently become a large field of study with multiple proposed materials and application methods. Such applications include in vivo drug delivery, disruption of bacterial cellular components and functions, as well as active components of treatment therapies such as photodynamic therapy and photothermal therapy. [17–23]

PDT and its effectivity on bacteria are especially important as bacteria develop higher levels of antibiotic resistance to current treatments. However, as previously stated, some of the major complications of PDT are the low concentration of the produced ROS, its ineffectiveness in human blood, and the localization of the photosensitizer.[14] To increase the concentration of ROS, nanomaterials have been proposed to be used in conjunction with photosensitizers due to their intrinsic properties such as nanoscale size, binding capabilities, surface plasmon resonance, photothermal properties, etc. depending on the nanomaterial. [17–23] Gold nanoparticles (AuNPs) have been examined for the enhancement of the PDT process in previous works and have been demonstrated to be an influential catalyst in the PDT process when used in combination with photosensitizers.[29–36]

Gold nanoparticles have specifically been investigated for use in PDT due to their optical properties, surface plasmon resonance, thiol chemistry, and enhanced permeability and retention in biological tissues.[29–36] Additionally, AuNPs are relatively easy to synthesize and characterize and are generally biocompatible making them viable for use in PDT.[37–40] AuNPs can be synthesized using a variety of methods including chemical reduction, electrochemical production, seeding growth, biological methods, ionic liquid production, and pulsed laser ablation in liquid

(PLAL).[38–40] Each process allows for the production of various sizes of AuNPs that absorb different wavelengths of light, which is essential for enhancing the PDT and PTT processes.

In addition to the ease of synthesis, the variety of characterization methods applicable for AuNPs facilitate further understanding to optimize them for application. Such characterization methods include transmission electron microscopy for size and morphological characterization, fluorescence spectroscopy, as well as zeta potentials which measure the surface charge of the AuNPs and reflect their stability in solution.[40] These analyses allow for the variation of the nanoparticles to modify their optical properties which can be harnessed to enhance the PDT process. By selecting a nanoparticle size and photosensitizer with relatively similar absorption wavelengths, the excitation of electrons and activation of the photosensitizer can be enhanced thereby generating higher concentrations of ROS.[37,41]

Another benefit of AuNPs, is that they have been shown in the literature to be relatively biocompatible as they have low cytotoxicity and do not induce the immune response and therefore present low risk for adverse complications.[31,37] It has similarly been demonstrated that AuNPs can be taken up by cells via pinocytosis or lysosomal bodies, indicating they are capable of entering hydrophilic intracellular spaces, a crucial component necessary for compounds involved in the PDT process.[37] By using photosensitizing agents in combination with AuNPs for PDT, it is hypothesized that higher concentrations of ROS can be localized at the site of treatment, thereby enhancing the effect of PDT.[37,41]

In this work, AuNPs were synthesized via pulsed laser ablation in an aqueous citrate solution. It has been demonstrated that laser ablation is an efficient, cost-effective, and eco-friendly method to synthesize AuNPs.[39] It has also been shown in the literature that it is possible to alter the

properties of various nanoparticles by altering the laser parameters; however there has been little data published regarding the impact of laser parameters on gold nanoparticles synthesized via PLAL which this work aims to explore. [42]

PLAL was specifically chosen for this work due to the biocompatibility of the generated AuNP samples. It has been discussed in the literature that chemical synthesized AuNPs can contain cytotoxic by-products or require isolation of the nanoparticles from toxic reagents such as gold chloride.[33,39] PLAL, on the other hand, can be used to directly synthesize AuNPs in solution without the need for strong reducing agents or toxic compounds allowing the samples to be used in biological applications immediately without sample preparation if the aqueous solvent is chosen correctly.[39] For example, aqueous sodium citrate, which was used in this work, can be used to stabilize the produced AuNPs while keeping the solution biocompatible.[43–45]

1.4 Bacterial Efflux Pumps

In addition to understanding the chemical and physical mechanism of PDT for the proposition of enhancements such as the incorporation of AuNPs, it is also crucial to consider the biochemical causes of antibiotic resistance to assist with the development of additional enhancements for the PDT process. It has been demonstrated that there are three main categories of mechanisms of antibiotic resistance. The first, minimizes antibiotic concentrations within the bacteria, the second modifies the antibiotic target through genetic mutations or post-translational modification, while the third directly inactivates the antibiotic via modification or hydrolysis.[46]

When applying this understanding to the PDT process, the most prevalent mechanism is the removal of compounds from within the bacterial cell. One of the most notable molecular mechanisms that decreases the concentration of antibiotics within the bacterial cell are bacterial

efflux pumps. Efflux pumps are integrated membrane proteins that span the membrane and act as a means for the cell to remove toxic substances from within the cell.[46–48] Substrates for these protein pumps include antibiotic compounds and photosensitizers. These proteins are encoded by an operon with a regulatory gene controlling their expression. Therefore, the presence of the efflux pump is intrinsic to the bacterial cell; however, increased antibiotic resistance is directly related to the over-expression of the efflux pump protein. Therefore, mutants that possess the over expression of efflux pumps are preferentially selected and can thereby proliferate the mutation.[46,47]

Efflux pumps are one of the primary ways that both gram-negative and gram-positive bacterial cells remove toxic compounds from their cellular matrix. Therefore, these proteins complexes have become a primary target in the effort of combating antibiotic resistance and enhancing the PDT process.[46–49] By developing compounds that inhibit or block these protein complexes, substances that are toxic to the bacterial cells, such as antibiotics or photosensitizers, can be localized within the cell for a longer duration, increasing the efficacy of the treatment method.[48,49] The efflux pump targeted in this work is the AcrAB-TolC complex found within the membrane of the gram-negative bacteria *Escherichia coli* (*E. Coli)*, the structure of which is depicted in Figure 2.[50–52]

The AcrAB efflux pump is a well-studied model efflux pump. It is specifically located in the inner membrane of *E. Coli* and consists of an AcrA, AcrB, and TolC subunits. The AcrB subunit pumps toxins from the cytoplasm to the periplasm where the TolC protein pumps the toxins from the periplasm to the extracellular space.[53–55] Such efflux pump proteins can be inhibited by various compounds including reserpine, cathinone, piperazine, and 5-Nitro-2-phenyl-1H-indole (INF-55) based on their binding affinities to a particular pump.[48,56] It is hypothesized that by doing so, the

photosensitizer can remain in the cytoplasm of the cell for a longer period of time, leading to a more effective photodeactivation process.

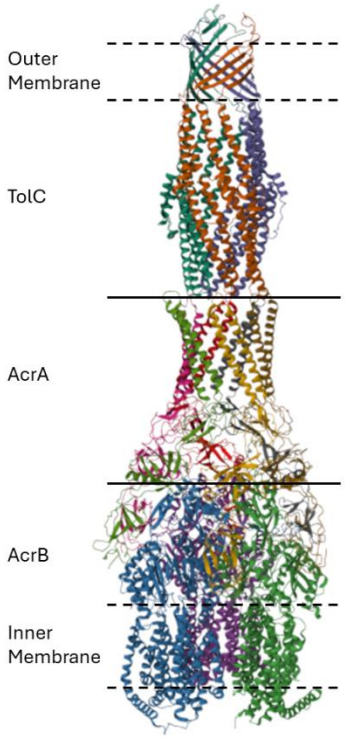

Figure 2: Structure and subunits of the E. Coli AcrAB-TolC Efflux Pump obtained from Research Collaboratory for Structural Bioinformatics Protein Data Bank. Solid lines separate the TolC, AcrA, and AcrB subunits. Dashed lines represent the inner and outer membrane.

By using the *E. Coli* AcrAB-TolC efflux pump as a model, the effectiveness of efflux pump inhibitors for the enhancement of the PDT process can be demonstrated. In this work, the molecular docking of the efflux pump inhibitor INF-55 was examined to lay the conceptual foundation for the proposed application of INF-55 in PDT. INF-55 is reported in the literature to be an efflux pump inhibitor of the NorA efflux pump in the gram-positive bacteria S. aureus.[48] Therefore, its effectivity as an inhibitor for the AcrB subunit of E. Coli has yet to be examined.

1.5 Project Summary

This work specifically examines the viability of enhancing the PDT process via the introduction of AuNPs and the efflux pump inhibitor INF-55. First, AuNPs were synthesized via PLAL and characterized to determine the most effective laser parameters for synthesis of the optimal AuNP solution. As this AuNP solution is proposed for a biological application, it is important to eliminate as many reducing agents, chemical stabilizers, and solution processing as possible. Hence, the use of PLAL in a sodium citrate solution for producing AuNPs in this work as opposed to traditional chemical synthesis methods such as the Turkevich method.[39,57]

Once the synthesis had been completed, ROS generation measurements were conducted to determine the optimal nanoparticle size as well as predict a possible mechanism for the enhancement of the PDT process. Next, molecular docking between the AcrB subunit and the photosensitizer methylene blue and the proposed efflux pump inhibitor, INF-55, were used to verify the viability of INF-55 to act as an effective inhibitor complex. Finally, AuNPs were tested in vitro on the gram-negative bacteria *E. Coli* to confirm the effectivity of nanoparticle enhanced PDT. This work helps establish the conceptual understanding of the viability and mechanism of the possible enhancement to the PDT process via the introduction of AuNPs and INF-55. Further experiments must be conducted to verify the viability of AuNPs and INF-55 when used together in vitro on *E. Coli*.

CHAPTER 2

METHODS AND MATERIALS

2.1 Synthesis of Gold Nanoparticles:

The AuNPs were synthesized via pulsed laser ablation in a 2 mM aqueous citrate solution. To do so, a gold target (99.99%, 0.250 mm thickness, GoodFellow) was fixed to an aluminum stage using double sided carbon tape and placed in a 50 mL beaker with a magnetic stir bar. Next, a sodium citrate solution was prepared as described in Appendix B, and 22 mL were added to the 50 mL beaker to achieve a solution height of 5 mm above the Au target. The 50 mL beaker was then placed on a magnetic stir plate which was located on a PI-MikroMove XYZ-stage. The beaker was covered with a 1 mm thick Pyrex petri dish cover to prevent splashing of the solution. This setup is depicted in Figure 3A.

The beam was focused using a 10 cm focusing lens and the target was raised to the focal point using the translational stage. The solution was ablated for 5 minutes. During the ablation period, the solution was stirred to prevent aggregation of the nanoparticles and the target was moved in the x and z directions using the translational stage at a speed of 10 mm/s as depicted in Figure 3B to vary the ablation location. Various laser parameters were tested, a summary of which can be found in table 1.

Nanosecond Pulse Rate	Sample 1	Sample 2	Sample 3
1064 nm	0.5 W	1.0 W	2.0 W
532 nm	0.5 W	1.0 W	2.0 W
Picosecond Pulse Rate			
1064 nm	20 kHz	30 kHz	50 kHz
532 nm	20 kHz	30 kHz	50 kHz

Table 1: Laser parameters used including pulse rate, wavelength, power, and frequency.

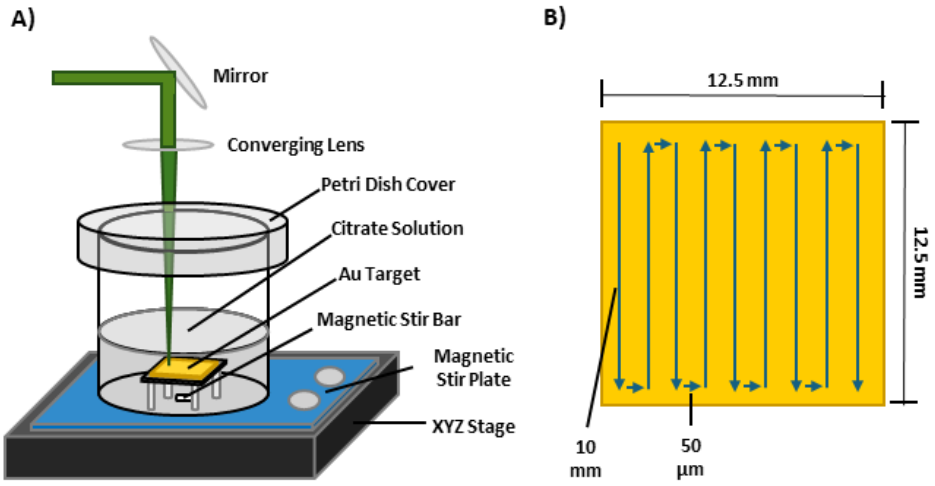

Figure 3: A) Experimental setup for the pulsed laser ablation in liquid for AuNP synthesis. B) Depiction of laser path during the ablation process.

2.2 Solvent Selection:

Prior to the analysis of various laser parameters, multiple aqueous solutions were examined for their effectivity in the PLAL synthesis of AuNPs and analyzed using transmission electron microscopy (TEM). Deionized (DI) water, ethanol, polyvinylpropylene (PVP), and sodium citrate were among the tested solutions using Picosecond, 532 nm, 40 kHz parameters. In both the DI water and ethanol solutions, the AuNPs were found to aggregate in solution which would limit their efficiency for the PDT process as seen in panels B and C of figure 4. Therefore, these solutions were eliminated. When using the PVP and citrate solutions, spherical AuNPs were obtained as seen in panels D and E of figure 4. However, the PVP solution was eliminated due to the relatively high viscosity of the solution which made the particles difficult to view, measure, and characterize. Therefore, aqueous sodium citrate was the solution of choice due to its ability to stabilize the AuNPs and prevent aggregation as well as its ease of use for synthesis and characterization.

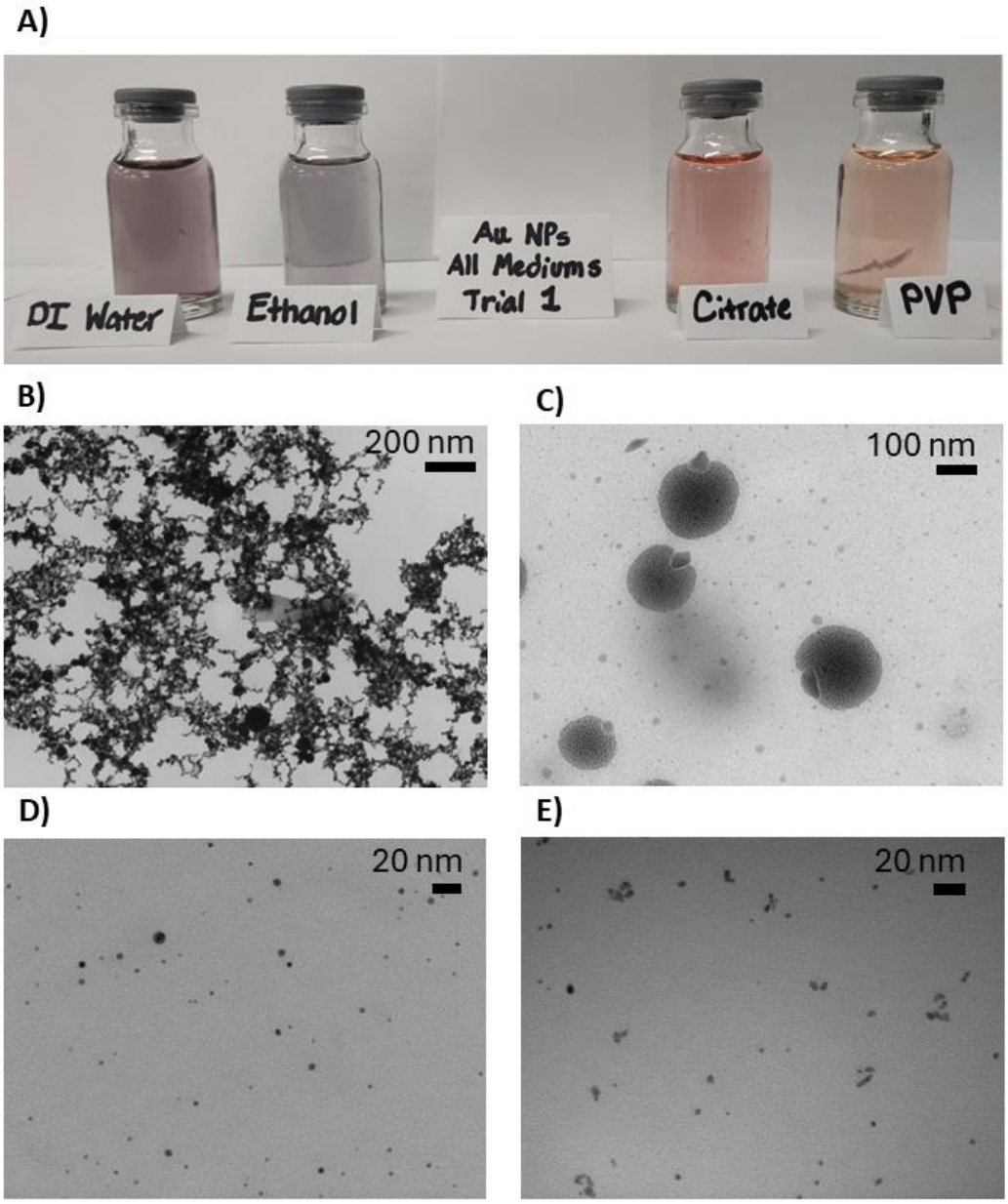

Figure 4: A) AuNPs synthesized in DI water, ethanol, aqueous PVP, and aqueous sodium citrate. TEM images of particle aggregation in DI water (B) and ethanol (C) and particle dispersion in aqueous PVP (D) and aqueous sodium citrate (E).

2.3 Characterization of Gold Nanoparticles:

As stated previously, the AuNP solutions were characterized by transmission electron microscopy. To prepare samples for TEM measurements, a drop cast technique was used. To do so, 3 μL of the AuNP solution was placed onto a 300-Mesh Copper TEM grid and allowed to dry. After the TEM images had been obtained, the program ImageJ was used to automatically measure the size of the produced AuNPs and obtain size distribution data. To do so, a Gaussian Blur was added to the images, the image contrast was decreased to mitigate background interference, the threshold was set to include the maximum number of nanoparticles, and the Feret diameter, ie. the longest particle dimension, was measured. These particle measurements were used to generate size distribution histograms and to calculate the average Feret diameter and standard deviation (n = 150) using the graphing program OriginPro. In addition to TEM characterization, the synthesized AuNPs were analyzed using UV-Visible Spectroscopy, Fluorescence Spectroscopy, and Fourier Transform Infrared (FTIR) Spectroscopy.

2.4 Reactive Oxygen Species Generation Measurement:

To verify and quantify the production of reactive oxygen species by the excitation of methylene blue in combination with AuNPs, the compound 9,10-Anthracenediyl-bis(methylene)dimalonic Acid (ABMDMA) was used in a colorimetric assay. ABMDMA has a peak absorbance at 400 nm. When in the presence of reactive oxygen species, ABMDMA undergoes a 2+4 cycloaddition of oxygen to form an endoperoxide. This cycloaddition results in a loss of the aromatic π-system of electrons leading to photobleaching of the optically observable properties.[58,59] Therefore, the absorbance of the solution directly corresponds to the ROS generated in solution.

Experimental solutions were prepared by combining the desired reagents, including MB (6.0×10^{-5} M), AuNPs, and INF-55 with 100 µL of a 2.4 mM ABMDMA solution in a 1.5 mL cuvette. The total volume was brought to a standard 1 mL using phosphate buffer solution (PBS). The initial absorbance was measured, and each cuvette was placed under irradiation for the allotted time. After irradiation, the absorbance was measured to verify the production of ROS.

2.5 Bacteria Photodeactivation:

To determine the effectiveness of AuNPs in combination with MB for PDT in vitro, the gram-negative bacteria *E. Coli* was irradiated both in the presence and absence of the various compounds. To do so, *E. Coli* was inoculated in LB Broth and allowed to grow for 18-24 hours at 37 °C with 200 rpm mixing. After the incubation period, the culture was diluted until an absorbance of ~1.7 at 600 nm was obtained which correlates to approximately 10^8 CFU/mL.

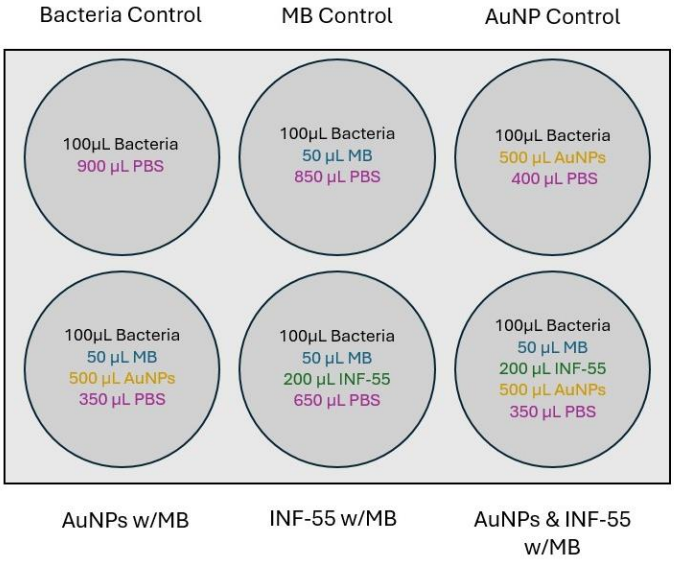

Figure 5: Volumes used in experimental photodeactivation solutions containing bacteria, methylene blue (MB), gold nanoparticles (AuNPs), 5-Nitro-2-phenyl-1H-indole (INF-55), and phosphate buffer solution (PBS).

Bacteria containing experimental solutions were prepared in a six well plate according to figure 5. The final concentrations of each compound tested were 0.03 μM MB, 0.025 mg/mL commercially produced AuNPs, 0.0095 mg/mL experimentally produced AuNPs and 8 μM INF-55. Once prepared, the plate was covered with aluminum foil to prevent unintended light exposure and was placed on a shaker plate and mixed at 100 rpm for 10 minutes. After the mixing time had elapsed, the aluminum foil was removed, and the plate was irradiated using a 660 nm red LED lamp (Bestqool, 105 W) for the allotted amount of time. The height between the lamp and the plate was maintained at 9 cm to ensure consistent fluence. This experimental setup can be seen in figure 6. After irradiation, each solution was serially diluted, plated, and allowed to incubate at 37 °C for 18-24 hours. After incubation, the colonies present on the plate were counted to determine cellular viability.

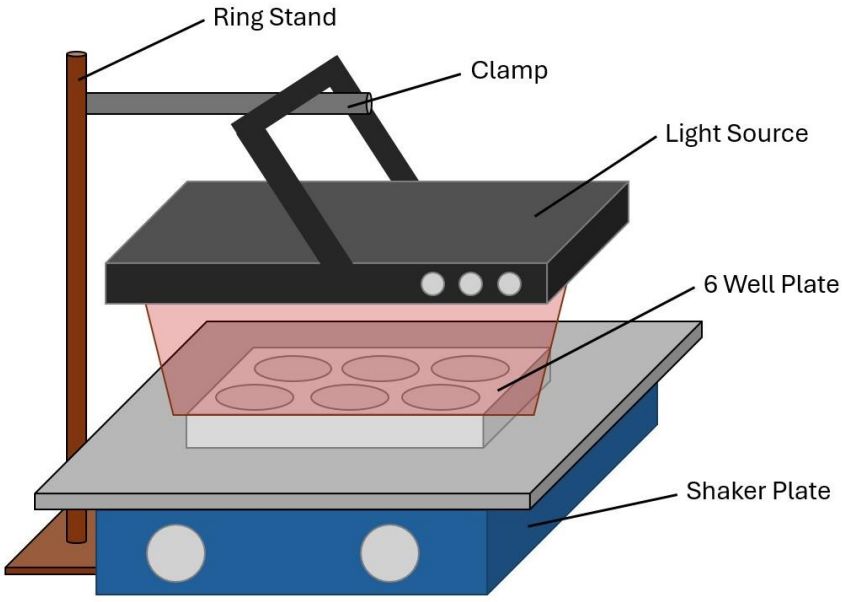

Figure 6: Photodynamic therapy bacteria deactivation experimental setup

2.6 Protein-Ligand Docking Modeling:

Molecular docking between the AcrB subunit and both MB and INF-55 was performed using Autodock Vina. The protein-ligand interactions determined using Autodock Vina were visualized using Discovery Studio 2021. The AcrB subunit amino acid sequence was obtained from the Protein Data Bank, and the ligand molecular structures were obtained from PubChem.

CHAPTER 3

RESULTS AND DISCUSSION

3.1 Size and Morphology of Gold Nanoparticles

The AuNPs were synthesized using various laser parameters and characterized using TEM as previously described in the materials and methods section. It was observed that each of the laser parameters resulted in spherical, disperse nanoparticles of various sizes. When considering the nanosecond pulse rate at the 1064 nm wavelength, it was determined that the average particle size when synthesized using 0.5 W, 1.0 W, and 2.0 W powers were 4.67 ± 2.66 nm, 4.60 ± 2.21 nm, and 4.67 ± 2.78 nm, respectively.

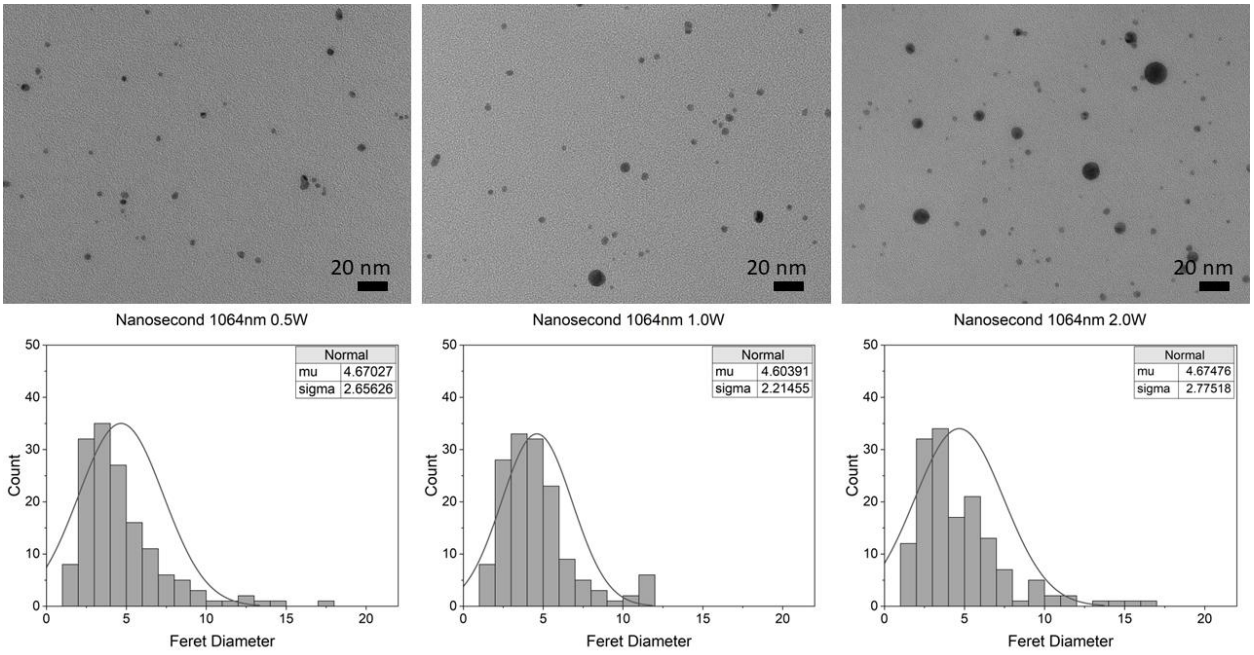

Figure 7: TEM images and size distribution graphs of AuNPs synthesized using the nanosecond pulse rate and 1064 nm wavelength at 0.5 W, 1.0 W, and 2.0 W powers.

By examining the TEM images, the 2.0 W power produced approximately double the number of nanoparticles when compared to the 0.5 W and 1.0 W powers which produced approximately the same number of nanoparticles. This observation was later confirmed using UV-Vis spectroscopy and will be discussed later in this work. Additionally, the 0.5 W and 2.0 W powers resulted in broader size distributions as compared to the narrow distribution obtained with the 1.0 W power.

Similarly, when AuNPs were synthesized using the nanosecond pulse rate at the 532 nm wavelength, the 0.5 W, 1.0 W, and 2.0 W powers resulted in average particle sizes of 6.44 $\pm$ 3.27 nm, 6.31 $\pm$ 2.44 nm, and 7.46 $\pm$ 3.28 nm, respectively. When compared to the 1064 nm AuNPs, the particles sizes obtained using the 532 nm wavelength were approximately 1.5 nm larger in Feret diameter and appeared more cylindrical or elongated.

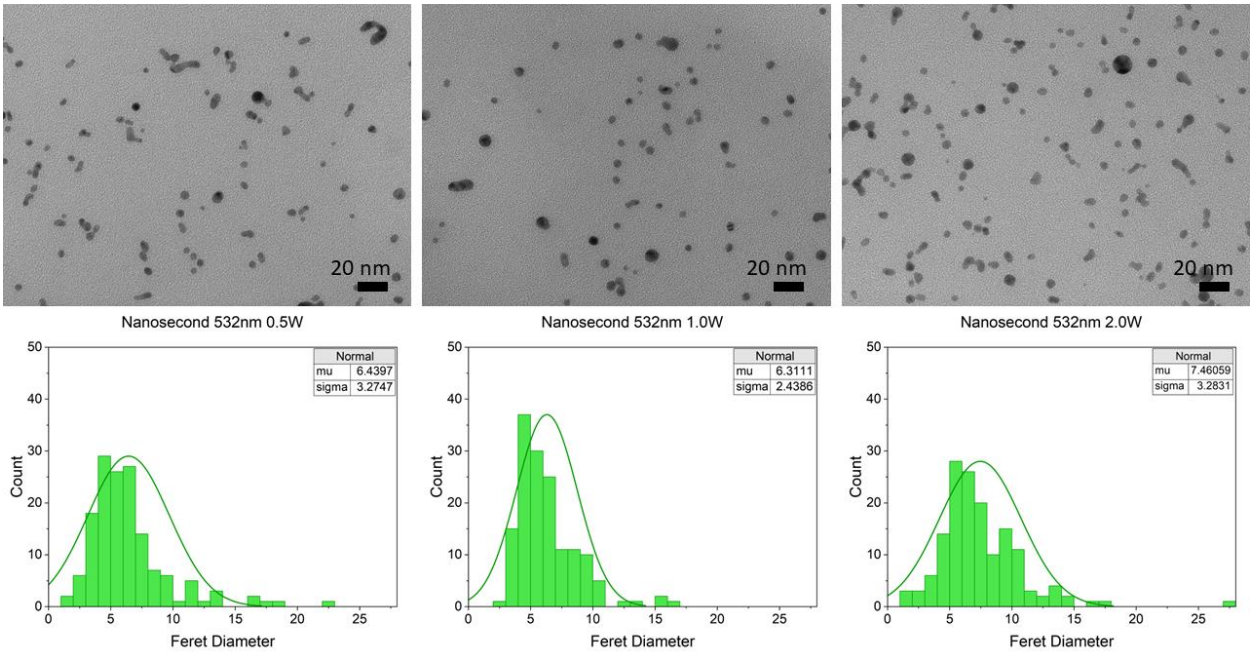

Figure 8: TEM images and size distribution graphs of AuNPs synthesized using the nanosecond pulse rate and 532 nm wavelength at 0.5 W, 1.0 W, and 2.0 W powers.

Similar to the observations between the various powers using the 1064 nm wavelength, when the AuNPs were synthesized using the 532 nm wavelength, the 2.0 W power produced approximately double the amount of nanoparticles as compared to the 1.0 W and 0.5 W powers. While the difference is not as drastic as with the 1064 nm wavelength, the 0.5 W and 2.0 W also produced a wider size distribution than the 1.0 W power. A significant difference from the 1064 nm wavelength is that the 2.0 W power at the 532 nm wavelength produced larger nanoparticles on average when compared to the 0.5 W and 1.0 W powers.

It has been demonstrated in the literature that as laser power increases, laser fluence (energy/area) increases, particle yield increases, and the average particle size decreases.[39,42] The described mechanism indicates that as the target material absorbs more energy, the generated plasma plume is larger resulting in higher particle yield and the larger particles can be fragmented producing smaller particles on average. However, most of these works used DI water as the ablation medium, which does not readily stabilize the produced nanoparticles, leading to fragmentation of larger particles. Therefore, it is possible that the stabilization due to the citrate solution assists in preventing large particle fragmentation, increasing the average particle size with increasing power as seen between the nanosecond 532 nm 0.5 W/1.0 W powers and the 2.0 W power.

When considering wavelength, it has been demonstrated that with metal targets such as gold, the closer the wavelength is to the surface plasmon resonance (SPR) wavelength of the metal, the deeper penetration into the material, resulting in a larger ablated mass per pulse, resulting in larger particles.[42] This is consistent with the results obtained from the 1064 nm and 532 nm nanosecond synthesis. The SPR wavelength of pure gold is approximately 530 nm.[60]

Therefore, the 532 nm wavelength is almost identical to the SPR wavelength, resulting in deeper target penetration, leading to larger particle production on average. However, deeper penetration is also likely to produce less uniform particles which can be seen in the TEM images of figure 8.

After examination of the nanosecond pulse rate, the picosecond pulse rate was tested at both the 1064 nm and 532 nm wavelengths with frequencies of 20 kHz, 30 kHz, and 50 kHz. Figure 9 depicts the results obtained for the picosecond 1064 nm wavelength.

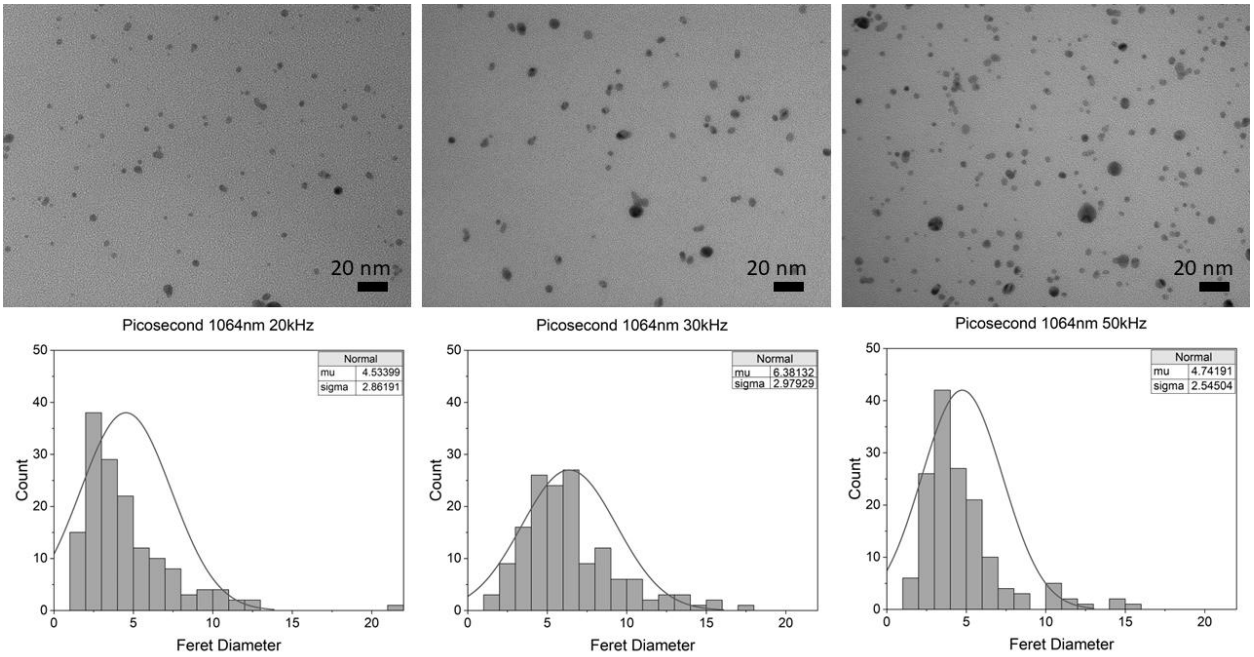

Figure 9: TEM images and size distribution graphs of AuNPs synthesized using the picosecond pulse rate and 1064 nm wavelength at 20 kHz, 30 kHz, and 50 kHz frequencies.

The average particle sizes obtained at 20 kHz, 30 kHz, and 50 kHz, were determined to be 4.53 ± 2.86 nm, 6.38 ± 2.98 nm, and 4.74 ± 2.54 nm respectively. By comparing the obtained TEM images, it was observed that the 50 kHz frequency resulted in the highest nanoparticle yield, with the 20 kHz frequency resulting in the second highest particle yield. This observation was later confirmed with UV-Vis spectroscopy. Interestingly, while the 30 kHz frequency

resulted in the lowest particles yield, it generated the largest average particle size. However, all frequencies produced comparable standard deviations.

When AuNPs were synthesized with the picosecond 532 nm wavelength, the average particle sizes for the 20 kHz, 30 kHz, and 50 kHz, frequencies were determined to be 4.85 ± 2.41 nm, 4.20 ± 1.53 nm, and 5.26 ± 3.60 nm, respectively.

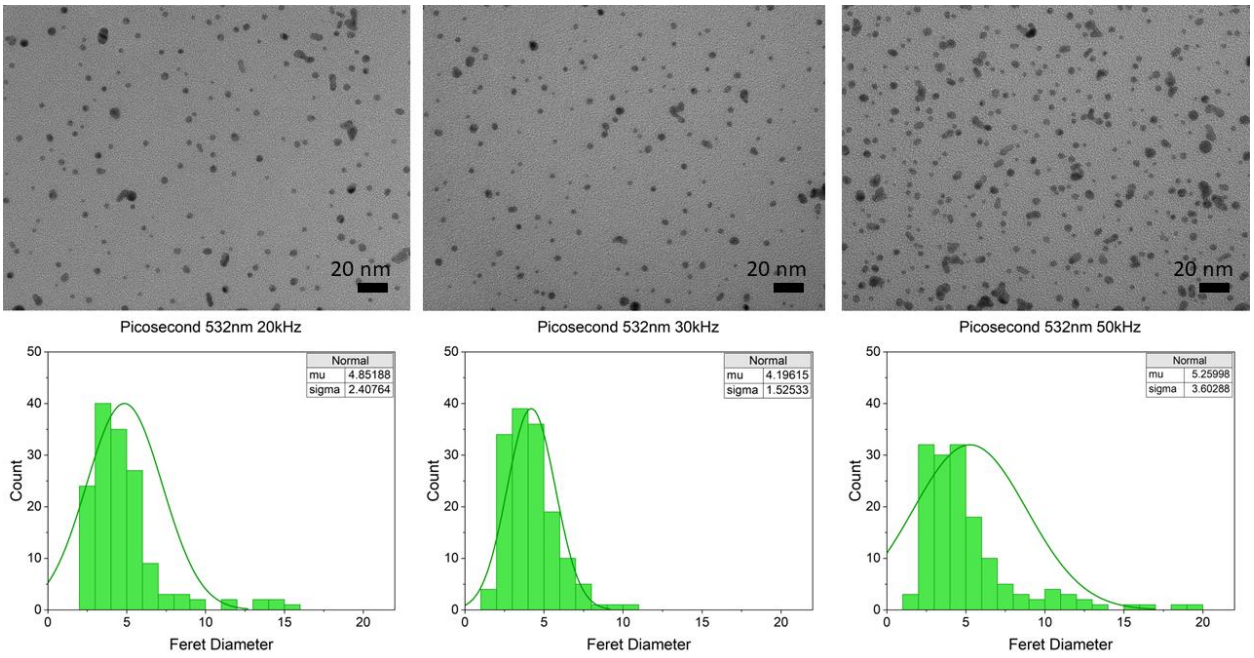

Figure 10: TEM images and size distribution graphs of AuNPs synthesized using the picosecond pulse rate and 532 nm wavelength at 20 kHz, 30 kHz, and 50 kHz frequencies.

Similar to the 1064 nm wavelength, when using the 532 nm wavelength, the 50 kHz frequency generated the highest particle yield while the 20 kHz frequency generated the second highest particle yield. However, when using the 532 nm wavelength, the 30 kHz frequency resulted in the smallest average particle size as opposed to the largest as was the case with the 1064 nm wavelength. Additionally, each frequency generated a distinct size distribution with 50 kHz resulting in the wider distribution and 30 kHz resulting in the narrower distribution.

When considering the variations in frequency, it could be predicted that as the repetition rate decreases, the fluence increases, resulting in higher nanoparticle yields.[42] However, some experimental works have shown higher yields at higher frequencies.[61] This inconsistency between the predicted effect and the observed effect is well represented in the obtained data in this work. With both the 1064 nm and 532 nm wavelengths, the 50 kHz frequency generated the higher concentration of AuNPs following the experimental trend, while the 20 kHz frequency generated the second highest concentration of AuNPs congruent with the predicted trend. The explanation behind the experimentally observed higher yields at higher frequencies, is that if the repetition rate is shorter than the diffusion rate, some nanoparticles may be fragmented resulting in higher yields and larger size distributions.[42]

When comparing the effect of wavelength, there did not appear to be any systematic increase or decrease in particle size between the 1064 nm and 532 nm wavelengths as was observed with the nanosecond laser. When comparing the difference between the nanosecond and picosecond pulse duration, there do not appear to be any major differences as the particle sizes obtained using the picosecond laser closely resembled that of the nanosecond 1064 nm wavelength. This similarity between the pulse durations is most likely due to the ablation mechanism.[39]

When considering the steps involved in the ablation process, thermal relaxation occurs before the end of the pulse as it occurs within a few tenths of a picosecond.[39] Therefore, both the picosecond and nanosecond pulse durations would have similar effects within the ablation process as the pulse duration is longer than the time it takes for the energy to transfer to the liquid medium. It could be predicted, however, that a femtosecond laser may provide different

results as the pulse duration would be shorter than the thermal-relaxation period, thereby allowing more of the energy to be converted to the target material as opposed to the surrounding medium.

3.2 Spectroscopic Characterization of AuNPs

As mentioned previously, UV-Visible spectroscopy was performed on the AuNP solutions to determine relative particle concentrations as well as verify the identity and purity of the AuNPs. Figure 11 depicts the UV-Vis spectra obtained for the AuNP samples produced using the nanosecond pulse rate.

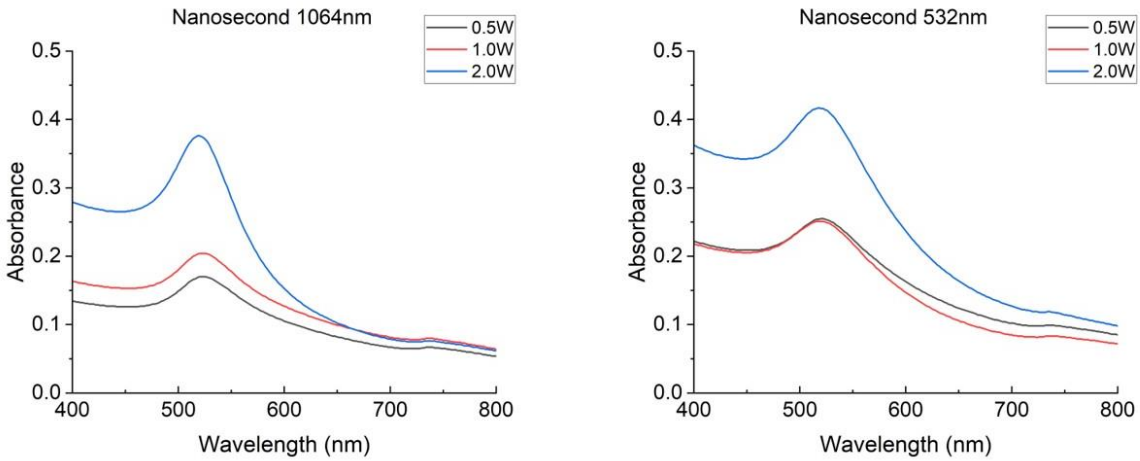

Figure 11: UV-Visible spectra for AuNP solutions obtained using nanosecond laser at 1064 and 532 nm wavelengths at 0.5 W, 1.0 W, and 2.0 W powers.

From these results, it is evident that each of the produced AuNP solutions had a peak wavelength within the 516-520 nm range which aligns with the SPR wavelength reported in the literature for nanoparticles ranging from 5-10 nm in diameter.[59,62] Additionally, these results confirmed the observations made from the TEM images that the 0.5 W and 1.0 W powers

produced relatively similar particle yields while the 2.0 W power produced almost double the amount of particles which is directly correlated to the absorbance of the solution.[62]

Figure 12 depicts the UV-Visible spectra for the samples synthesized using the picosecond laser. Similar to the nanosecond pulse duration, the SPR wavelengths for each solution fell within the 516-520 nm range, again correlating with nanoparticles ranging from 5-10 nm in diameter.[59,62] Additionally, the absorbances of the samples produced using the picosecond laser at both the 1064 nm and 532 nm wavelengths confirmed the approximate nanoparticle concentrations observed in the TEM images. For both wavelengths, the 50 kHz frequency produced the highest particle yield, followed by the 20 kHz frequency, and then the 30 kHz frequency.

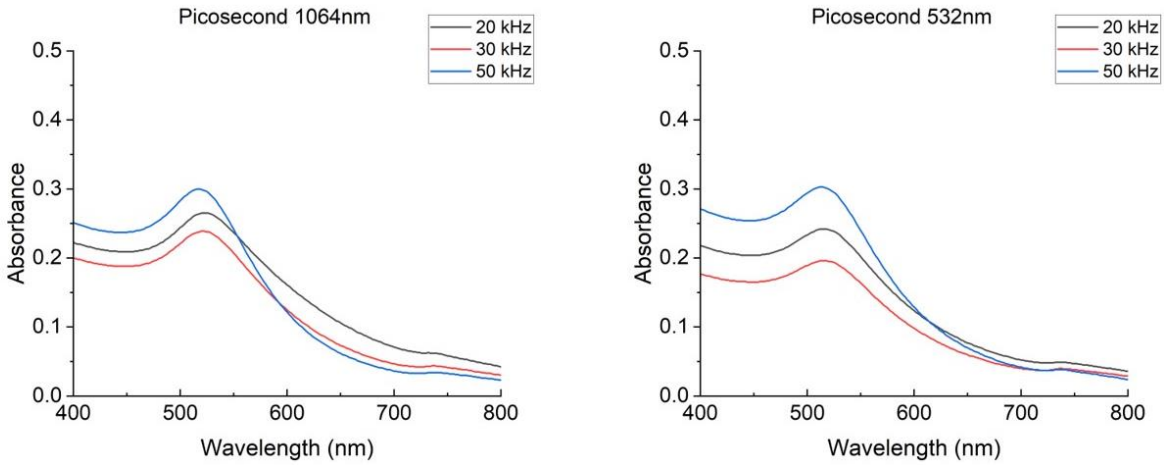

Figure 12: UV-Visible spectra for AuNP solutions obtained using picosecond laser at 1064 and 532 nm wavelengths at 20 kHz, 30 kHz, and 50 kHz frequencies.

In addition to UV-Visible spectroscopy, fluorescence spectra for each solution were obtained using an excitation wavelength of 518 nm. Figure 13 depicts the combined fluorescence spectra for the solutions obtained using the nanosecond and picosecond lasers. The most notable information obtained from these spectra is the secondary conformation of the presence and identity

of the AuNPs in solution. As the SPR wavelength was determined to be approximately 518 nm, it would be expected that if the solution did in fact contain AuNPs, the peak fluorescence would be red shifted by approximately 40-60 nm from the peak absorbance wavelength due to Stokes shifting.[63] For each solution, this primary peak shift was observed at approximately 560-570 nm. Additional peaks were also observed at approximately 580, 585, and 595 nm. These additional peaks are most likely due to the size variation of the AuNPs in solution as different sized AuNPs will experience a different Stokes shift.[63] Therefore, samples with fewer fluorescent peaks would most likely have more uniform particles.

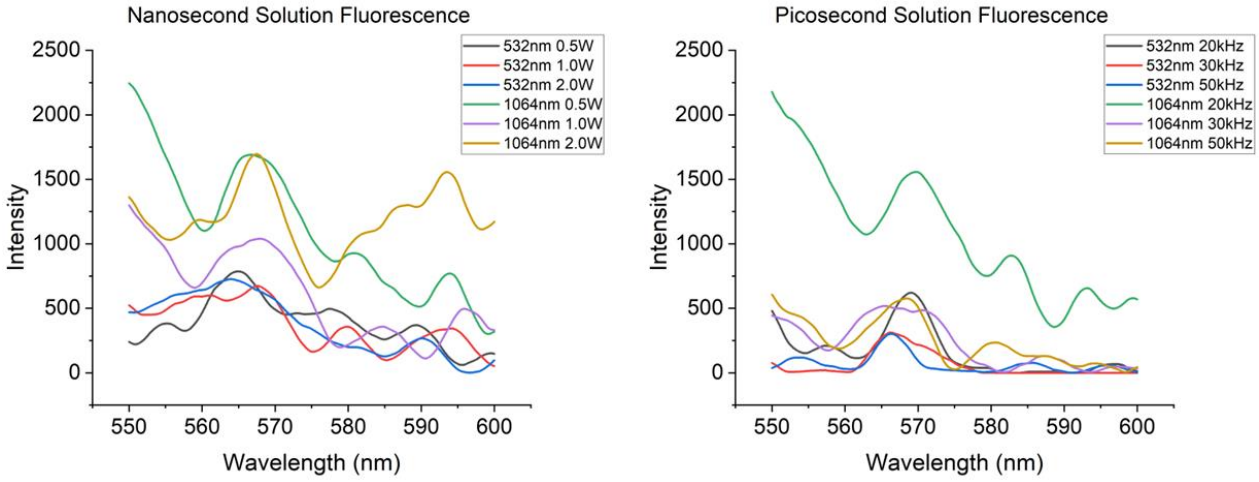

Figure 13: Fluorescence spectra for AuNP solutions obtained using nanosecond and picosecond laser with 1064 and 532 nm wavelengths at various powers and frequencies.

The final spectroscopic analysis used to characterize the produced AuNPs was FTIR measurements. As each of the solutions were produced in a 2 mM sodium citrate solution, it would be predicted that FTIR signals would be present for a pure citrate solution and decreased in the AuNP solutions if citrate had adsorbed onto the surface of the nanoparticles which results in

stabilization. Figure 14 depicts the FTIR spectra for the AuNP solutions synthesized using the nanosecond pulse duration.

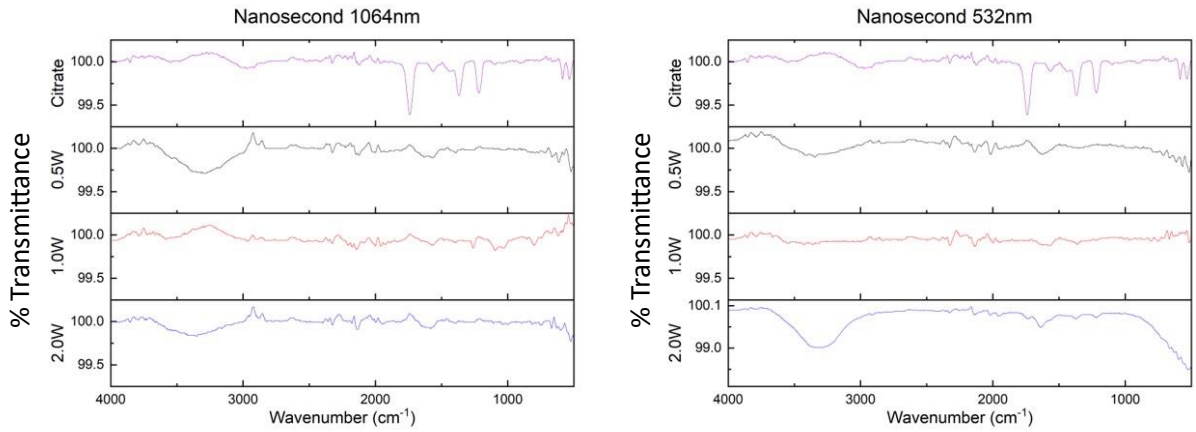

Figure 14: FTIR spectra for AuNP solutions obtained using nanosecond laser at 1064 and 532 nm wavelengths at 0.5 W, 1.0 W, and 2.0 W.

As predicted, the citrate peaks located at approximately 1750 cm^{-1}, 1450 cm^{-1}, 1300 cm^{-1}, are no longer present in the spectra obtained for the AuNP solutions indicating either the adsorption, destruction, or modification of citrate. Additionally, an OH stretch around 3400 cm^{-1} becomes prevalent in the spectra for the 0.5 W and 2.0 W solutions. It has been demonstrated in the literature that various mechanisms for the binding between citrate and the metal surface can occur.[43] The structure of citrate contains three carboxy groups and one hydroxy group as seen in figure 15, each of which can form bonds with the metal surface via oxygen.[43]

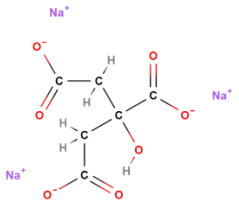

Figure 15: Chemical structure of sodium citrate generated using MolView.

Therefore, the binding mechanism between citrate and the AuNPs formed during ablation must vary based on the laser parameters used. For the 1.0 W powers, the hydroxy group may be bound to the surface of the nanoparticles, preventing the formation of an OH stretch at 3400 cm^{-1}. The 0.5 W and 2.0 W powers, on the other hand, must primarily bind via the carboxy groups leaving a dangling hydroxy group which can be detected via IR spectroscopy at 3400 cm^{-1}. When examining the solutions synthesized using the picosecond laser, the FTIR spectra shown in figure 16, also demonstrates citrate adsorption or modification.

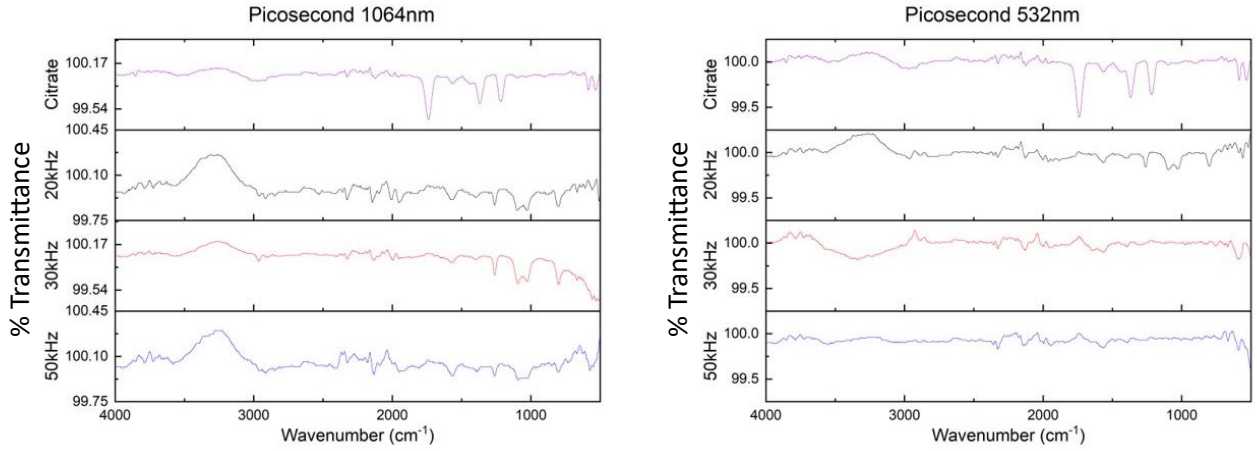

Figure 16: FTIR spectra for AuNP solutions obtained using picosecond laser at 1064 and 532 nm wavelengths at 20 kHz, 30 kHz, and 50 kHz.

3.3 Reactive Oxygen Species Production

To understand the probable mechanism of bacteria deactivation, the ROS yield was measured via spectroscopic analysis of the photobleaching of 9,10-Anthracenediyl-bis(methylene)dimalonic Acid (ABMDMA) as previously explained in the methods and materials section. The obtained results are reflected in figure 17. First, the effect of nanoparticle size was examined utilizing standardized, commercially produced nanoparticles of three different

sizes: 10, 20, and 40 nm as seen in figure 17A. Based on the obtained data, it is evident that the presence of AuNPs enhances the photobleaching of ABMDMA, which is directly correlated with an increased concentration of produced ROS.[56,57] In addition to the increased production of ROS with the addition of AuNPs, it can be concluded that as particle size decreases, the ROS production increases. With nanomaterials, increased catalytic yields are often correlated to the increase in the surface area to volume ratio with a decrease in particle size.[64,65] Therefore, it can be predicted that smaller nanoparticles would be more effective in enhancing the PDT process. However, it is important to consider that as particle size decreases, the ease of circulation of the nanoparticles within biological systems increases despite site directed localization.[66]

When selecting the optimal experimentally produced nanoparticle solution, the nanosecond, 532 nm, 2.0 W solution was selected for further examination during the in vitro PDT process, as even though smaller particle sizes produce higher ROS yields, it is also crucial to limit adverse effects. Therefore, selecting a solution with an average particle size of 7.46 as opposed to 4.5 or even 6 can allow for a high ROS yield while limiting enhanced systematic distribution.

After the effect of particle size had been examined and the optimal experimentally obtained nanoparticle solution had been selected, both the experimental AuNP solution and the proposed efflux pump inhibitor, INF-55, were tested for their impact on the ROS generation as seen in figure 17B. Based on the obtained data, INF-55 with methylene blue alone did not have a major impact on the ROS concentration. The experimentally obtained AuNP solution did result in an increased ROS generation; however, the most significant increase in ROS generation resulted from the combination of the experimental AuNPs and INF-55. This indicates that the

combination of both AuNPs and INF-55 should enhance the ROS yield, resulting in a more effective PDT process.

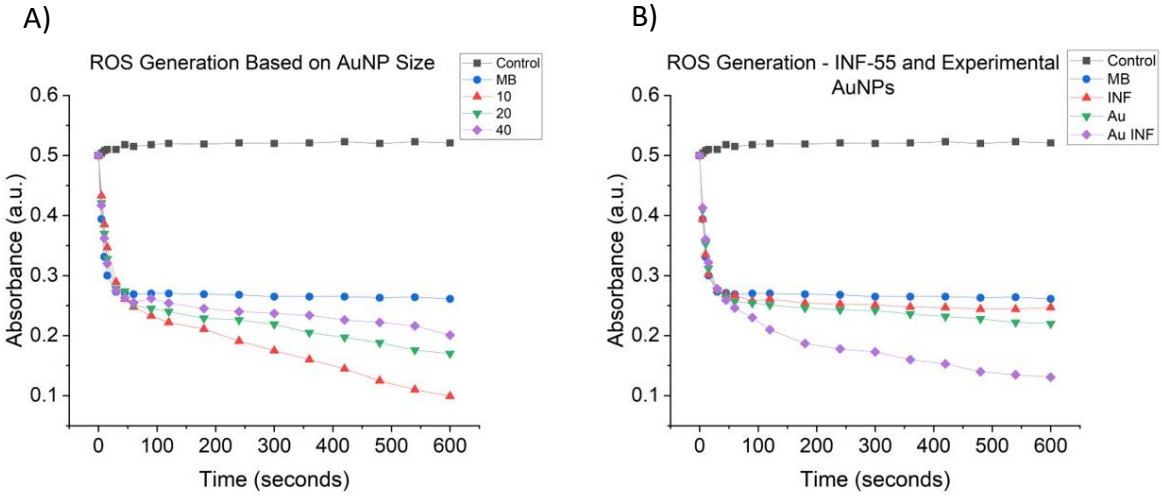

Figure 17: ROS generation measurements via monitoring of the photobleaching of ABMDMA. Control: PBS + ABMDMA, MB: PBS + MB + ABMDMA, 10/20/40: PBS + MB + AuNPs (size 10, 20, and 40 nm) + ABMDMA, INF: PBS + MB + INF-55 + ABMDMA, Au: PBS + MB + experimental AuNPs + ABMDMA, Au INF: PBS + MB + INF-55 + experimental AuNPs + ABMDMA.

3.4 INF-55 and Methylene Blue Docking Analysis

To predict the viability of INF-55 as an inhibitor of the AcrB component of the *E. Coli* AcrAB-TolC efflux pump, molecular docking was performed using Autodock Vina as described in the materials and methods section. The AcrB subunit has been predicted to be the primary binding site for ligand transport.[46-49] As the AcrB is a homotrimeric antiporter, a single polypeptide unit was isolated for the docking calculations. The overall structure of the AcrB subunit and the isolation of the polypeptide unit is represented in figure 18.

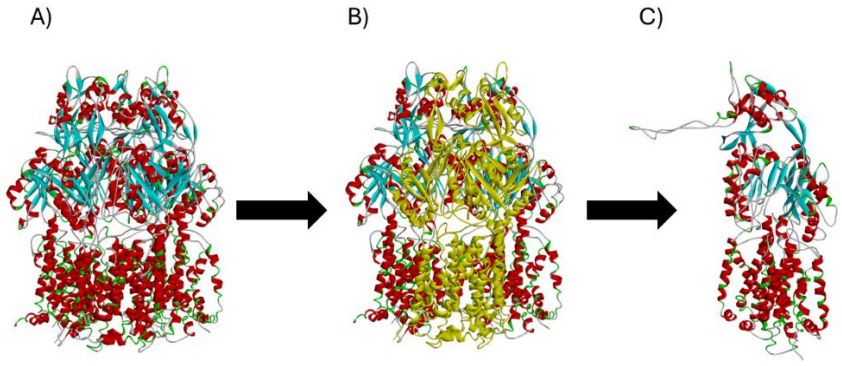

Figure 18: The three-dimensional structure of the A) AcrB subunit, B) single polypeptide unit within the trimer, and C) isolated polypeptide unit.

After the isolation of a single polypeptide unit, the binding affinity of the best 9 modes for both MB and INF-55 were calculated using Autodock Vina and are summarized in table 2. These results indicate that each of the INF-55 binding modes has a higher binding affinity than the binding modes for MB. Therefore, INF-55 would most likely be preferentially selected by the AcrB component, acting as a competitive inhibitor and preventing the binding and subsequent removal of MB via the efflux pump mechanism.

Ligand Binding Affinity (kcal/mol)									
Ligand	Mode 1	Mode 2	Mode 3	Mode 4	Mode 5	Mode 6	Mode 7	Mode 8	Mode 9
INF-55	-9.1	-9.0	-8.9	-8.6	-8.5	-8.1	-8.1	-8.1	-7.9
MB	-7.2	-7.1	-7.0	-7.0	-6.9	-6.7	-6.6	-6.6	-6.5

Table 2: Ligand binding affinities bewteen MB or INF-55 and the AcrB component of the AcrAB-TolC bacterial efflux pump.

After the binding affinities had been calculated, the specific interactions between the amino acid residues and the ligands were modeled both two- and three-dimensionally. The binding mode with the highest affinity for both MB and INF-55 is represented in figure 19.

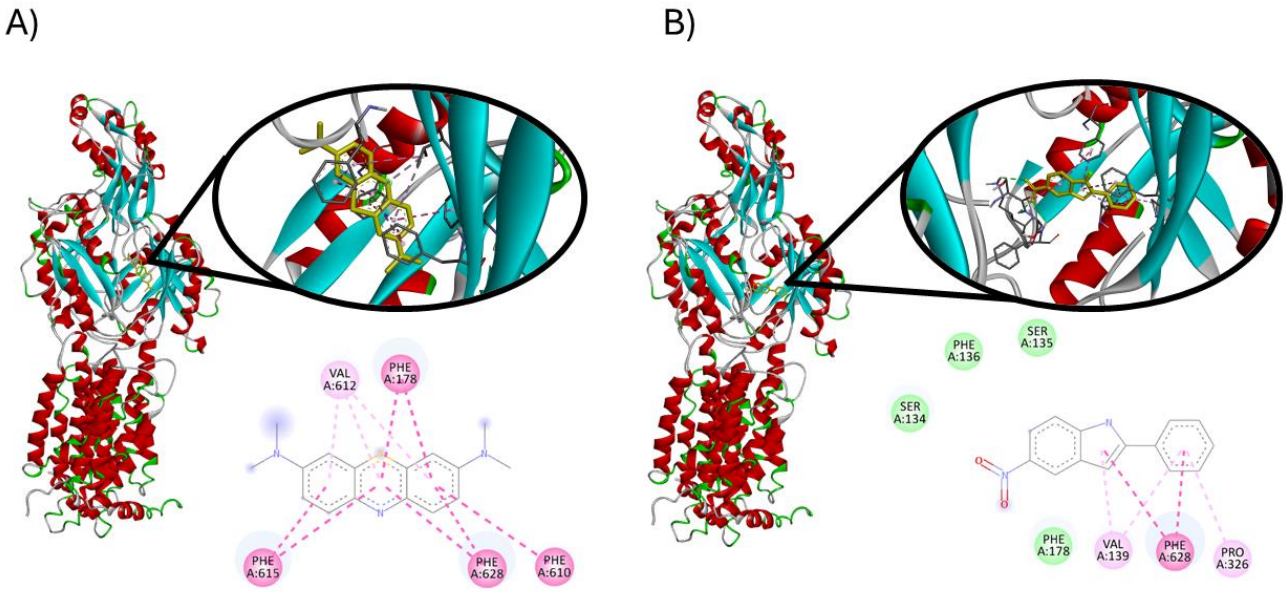

Figure 19: Two- and three-dimensional representations of the highest affinity binding modes of A) methylene blue and B) INF-55. Light pink interactions represent Pi-Alkyl interactions, dark pink interactions represent Pi-Pi stacking interactions, and green interactions represent Van der Waals forces.

Based on this information, it is evident that INF-55 interacts with SER134, SER135, PHE136, and PHE178 via Van der Waals interactions, VAL139 and PRO326 via Pi-Pi stacking, and the PHE628 via Pi-alkyl interactions. Additionally, each functional group of the INF-55 compound is stabilized by at least two amino acid residues. The nitro group is stabilized by SER134, SER135, PHE136, and PHE178, the pyrrole ring is stabilized by VAL139 and PHE628 and the phenyl group is stabilized by PHE628 and PRO326. MB, on the other hand, is only centrally stabilized via Pi-Pi stacking with the conjugated Pi system by the residues PHE178, PHE615, PHE628, PHE610, and a Pi-alkyl interaction via VAL612. This provides additional evidence that INF-55 has stronger binding interactions than MB. Additional two- and three-

dimensional binding interactions for the top 3 binding modes for both INF-55 and MB can be found in Appendix A.

The previously identified residues have been isolated in the literature as the main amino acids involved in the ligand binding in the drug binding pocket of the AcrB component.[56,67–70] Multiple ligands including doxorubicin, minocycline, and ciprofloxacin, ethidium bromide, reserpine, and methylene blue have been shown to interact with these residues, indicating that INF-55 could, in fact, bind to the AcrB subunit in the drug binding pocket. One of the primary residues involved in virtually every protein-ligand interaction in both the literature as well as the additional binding modes for MB and INF-55 found in Appendix A, is PHE628. It is possible that PHE628 is one of the primary binding residues when it comes to drug efflux via the AcrB subunit. Therefore, compounds such as INF-55 that interact strongly with PHE628 could act as competitive inhibitors for the AcrB subunit.

3.5 Bacteria Photodeactivation

The final aspect examined in this work was the in vitro photodeactivation of the gram-negative bacteria *E. Coli* when using various size AuNPs. As discussed previously, it was determined that smaller gold nanoparticles produced higher ROS yields. Therefore, it could be predicted that as particle size decreases, the PDT effectivity should increase. This correlation was directly represented in the photodeactivation data obtained and represented in Figure 20 when standardized, commercially produced nanoparticles of 10, 20, and 40 nm diameters were used.

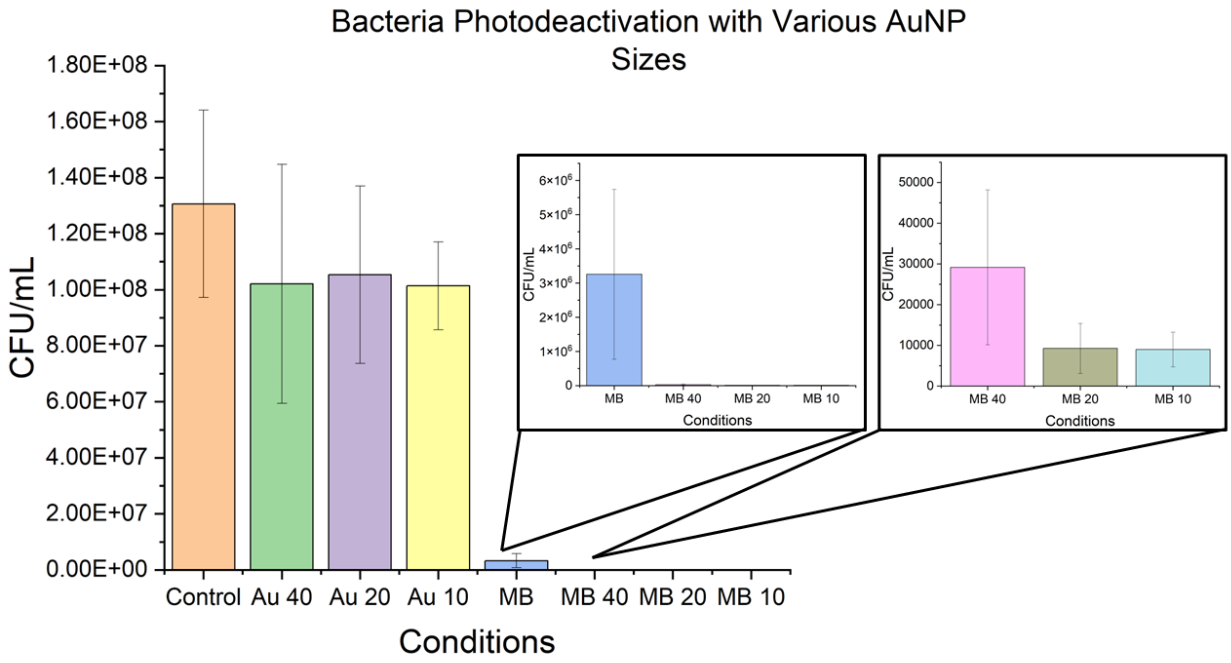

Figure 20: Bacteria concentrations in colony forming units (CFU)/mL after 5 minutes of irradiation using MB and various AuNP sizes. Control: bacteria + PBS, Au 40/20/10: bacteria + PBS + AuNPs (40, 20, or 10 nm in diameter), MB: bacteria + PBS + MB, MB 40/20/10: bacteria + PBS + MB + AuNPs (40, 20, or 10 nm in diameter).

The effectivity of the PDT procedure was determined by counting the colony growth after irradiation and serial dilution, thereby allowing for the calculation of bacteria concentration after irradiation. It was determined that after 5 minutes of irradiation with no photosensitizer, or AuNPs, the bacteria concentration was approximately $1.31 \times 10^8 \pm 3.34 \times 10^7$ CFU/mL. When 40, 20, and 10 nm AuNP sizes were used independent of MB, bacteria concentrations of $1.02 \times 10^8 \pm 4.26 \times 10^7$ CFU/mL, $1.05 \times 10^8 \pm 3.17 \times 10^7$ CFU/mL, and $1.01 \times 10^8 \pm 1.57 \times 10^7$ CFU/mL which correlates to 22.14 %, 19.85 %, and 22.90 % decreases, respectively. When MB is introduced independently, a bacteria concentration of $3.26 \times 10^6 \pm 2.48 \times 10^6$ CFU/mL was obtained indicating a 97.51% decrease

from the control group. When MB was used in combination with 40, 20, and 10 nm AuNPs, the bacteria concentration was determined to be $2.91 \times 10^4 \pm 1.90 \times 10^4$ CFU/mL, $9.25 \times 10^3 \pm 6.13 \times 10^3$ CFU/mL, and $8.97 \times 10^3 \pm 4.24 \times 10^3$ CFU/mL indicating percent decreases of 99.98 %, 99.99 %, and 99.99 %, respectively.

These results clearly indicate that AuNPs, when used in combination with the photosensitizer methylene blue, results in almost complete termination of bacteria after only 5 minutes of irradiation. Preliminary experiments utilizing the experimentally produced AuNPs via the nanosecond 532 nm 2.0 W laser parameters yielded a percent difference of 99.09 % when compared to the control. The final concentration of the commercially produced nanoparticles was 0.025 mg/mL while the final concentration of the experimentally produced nanoparticles was 0.0095 mg/mL as this was the maximum yield of the PLAL procedure. This variation in concentration is the most likely cause of the slight reduction in efficacy in the PDT process between the experimentally synthesized AuNPs. Currently, experiments involving the use of INF-55 in combination with MB and experimentally produced AuNPs have produced inconclusive results. Therefore, future experiments should be conducted to understand the impact in vitro of the incorporation of the efflux pump inhibitor INF-55.

CHAPTER 4

CONCLUSION

This project was designed to understand the fundamental concepts behind the incorporation of gold nanoparticles and the efflux pump inhibitor, INF-55, to enhance the photodynamic therapy process. It was determined that the laser parameters that produced the optimal size nanoparticles for this application were the nanosecond pulse duration, 532 nm wavelength, and 2.0 W power. These parameters resulted in an average particle size of 7.46 $\pm$ 3.28 nm. It was also observed by monitoring the photobleaching of ABMDMA, that smaller nanoparticle sizes increased the ROS yield during irradiation, while INF-55 alone has no direct impact on the ROS generation. Molecular docking confirmed the viability of INF-55 to act as a competitive inhibitor of MB to the AcrB efflux pump subunit as the primary binding mode of INF-55 had a binding affinity of -9.1 kcal/mol while the binding affinity of the primary binding mode of MB was -7.2 kcal/mol. Finally, when tested in vitro, the combination of AuNPs with MB resulted in a 99.98 - 99.99% reduction in the concentration of bacteria after 5 min irradiation indicating that the incorporation of AuNPs does, in fact, enhance the PDT process. Future work should examine the use of INF-55 in vitro to determine if it has any impact on the effectivity of the PDT process.

APPENDIX A: ADDITIONAL EXPERIMENTAL DATA

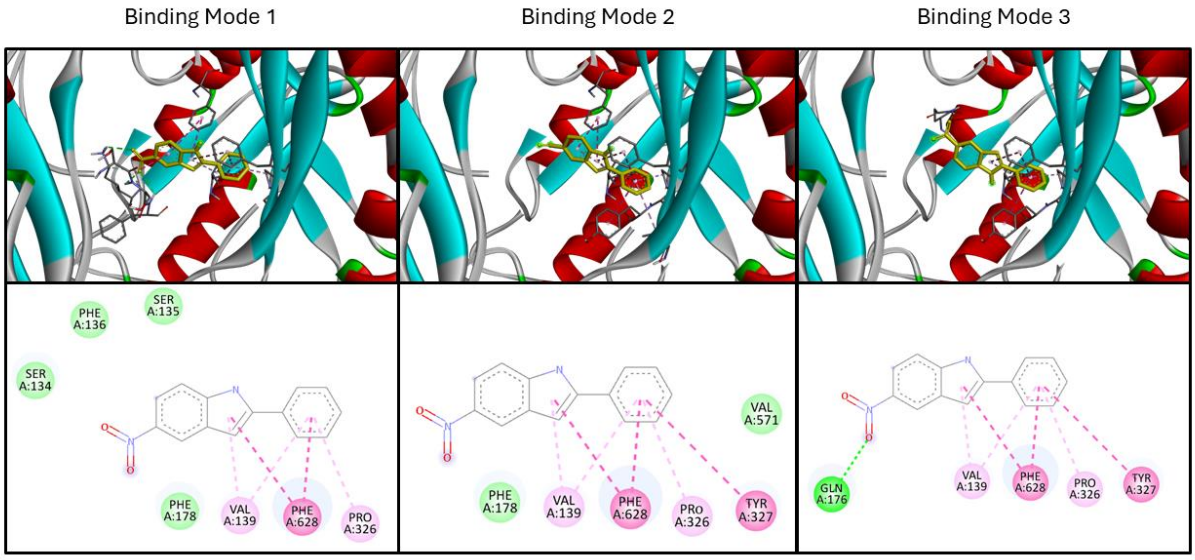

Appendix A - Figure 1: Two- and three-dimensional representations of the three highest affinity binding modes of INF-55. Light pink interactions represent Pi-Alkyl interactions, dark pink interactions represent Pi-Pi stacking interactions, and green interactions represent Van der Waals forces.

Appendix A - Figure 1 shows the two- and three-dimensional interactions between the three most energetically favorable binding modes of INF-55 and the AcrB subunit of the AcrAB-TolC efflux pump found in the gram-negative bacteria *E. Coli* as referenced in section 3.4. Modes 1 through 3 were calculated to have binding affinities of -9.1, -9.0, and –8.9 kcal/mol respectively and each show interactions between PHE628, which was the predicted primary amino acid residue involved in ligand binding.

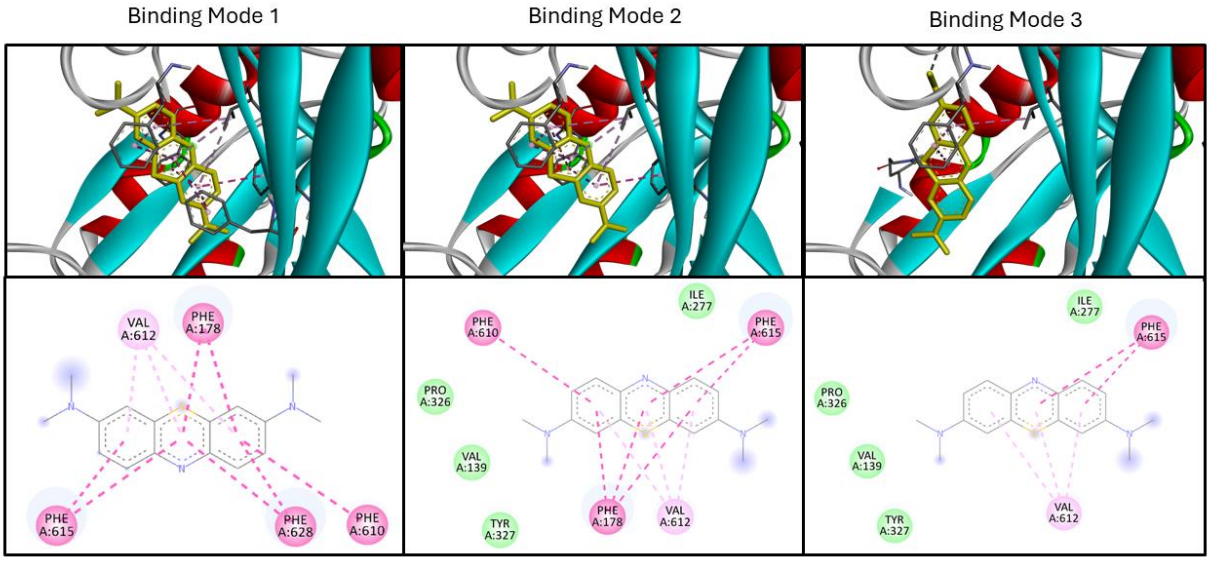

Appendix A - Figure 2: Two- and three-dimensional representations of the three highest affinity binding modes of INF-55. Light pink interactions represent Pi-Alkyl interactions, dark pink interactions represent Pi-Pi stacking interactions, and green interactions represent Van der Waals forces.

Appendix A - Figure 2 represents the two- and three-dimensional interactions between the three most energetically favorable binding modes of MB and the AcrB subunit of the AcrAB-TolC efflux pump found in the gram-negative bacteria *E. Coli* as discussed in section 3.4. Modes 1 through 3 were calculated to have binding affinities of -7.2, -7.1, and –7.0 kcal/mol respectively, each of which are lower than the 9 highest affinity binding modes of INF-55.

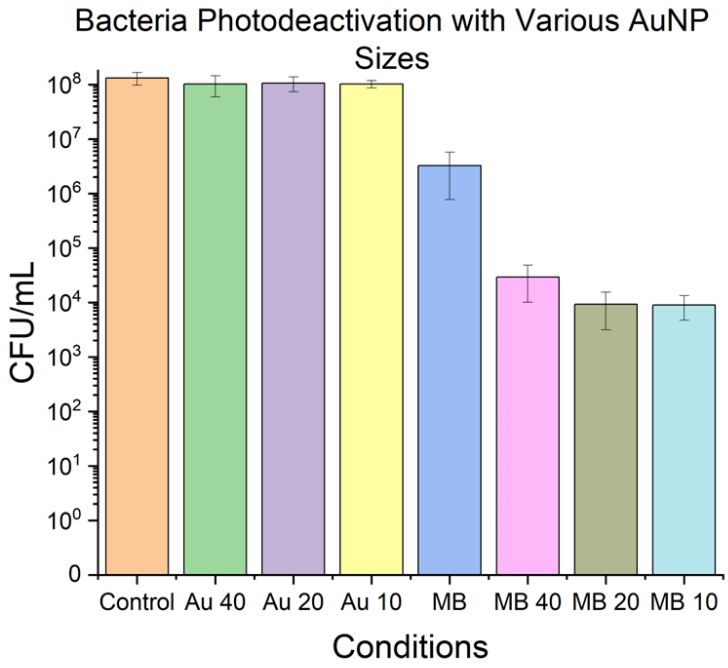

Appendix A - Figure 3: Bacteria concentrations in colony forming units (CFU)/mL after 5 minutes of irradiation using MB and various AuNP sizes represented on a logarithmic scale. Control: bacteria + PBS, Au 40/20/10: bacteria + PBS + AuNPs (40, 20, or 10 nm in diameter), MB: bacteria + PBS + MB, MB 40/20/10: bacteria + PBS + MB + AuNPs (40, 20, or 10 nm in diameter).

The bacteria photodeactivation data used to generate figure 20 in section 3.5 can also be represented with a logarithmic scale on the CFU/mL axis. Each major tick on the y-axis represents a 10-fold decrease in bacteria concentration. Appendix A - Figure 3 can be used to better visualize the relative effect of the tested parameters.

APPENDIX B: SAMPLE PREPARATIONS AND ADDITIONAL PROCEDURES

i. Preparation of methylene blue stock solution (6.1×10^{-4} M)

To obtain a stock solution of methylene blue, 1.140 g of crystalline methylene blue (MB • $3H_2O$, MW = 373.90 g/mol, Sigma Aldrich) was weighed out using an electronic scale (0.1 mg sensitivity). The compound was placed in a 50 mL centrifuge tube and 50 mL of Autoclaved DI water was added and shaken to dissolve. The centrifuge tube was covered with aluminum foil to prevent photobleaching.

ii. Preparation of methylene blue experimental solution (6.1×10^{-5} M)

Experimental solutions of methylene blue were generated by taking 5 mL of the MB stock solution (6.1×10^{-4} M) and placing it in a 50 mL centrifuge tube. Next. 45 mL of Autoclaved DI water were added to dilute the solution to a final concentration of 6.1×10^{-5} M. Similar to the stock solution, the experimental solution tube was covered with aluminum foil to prevent photobleaching.

iii. Preparation of sodium citrate solution (2 mM)

A 2 mM solution of aqueous sodium citrate was prepared by weighing out 588.2 mg of sodium citrate (MW = 294.09 g/mol, Fisher) and placing it in a 1,000 mL volumetric flask. Next, 1,000 mL of DI water was added to the mark. The solution was stirred using a magnetic stir bar and magnetic stir plate until the sodium citrate was completely dissolved. The solution was placed in a 1 L screw-top bottle and stored at room temperature for use in pulsed laser ablation.

iv. Preparation of phosphate buffer solution (pH = 7.4)

To prepare the phosphate buffer solution, 0.2108 g of potassium phosphate monobasic (MW = 136.09 g/mol, ≥ 99.0%, Sigma Aldrich), 0.729 g of sodium phosphate dibasic (MW = 141.96 g/mol, ≥ 99.0%, Sigma Aldrich), and 9.0054 g of sodium chloride (MW = 58.44 g/mol BioXtra, ≥ 99.5%, Sigma Aldrich) were weighed out and placed in a 1,000 mL volumetric flask. DI water was added to the mark, and the solution was stirred using a magnetic stir bar and magnetic plate until completely dissolved. Next, the solution was placed in a 1 L screw-top bottle and autoclaved for ~60 minutes (Liquid15 Cycle).

v. Preparation of INF-55 solution:

To prepare a 20 µM solution of INF-55, 0.008 g of INF-55 (MW = 238.25 g/mol, Millipore Sigma) was weighed out and dissolved in 500 µL of DMSO in a 50 mL centrifuge tube. Next, 49.5 mL of Autoclaved DI water was added to the centrifuge tube. The solution was mixed by shaking and the tube was covered with aluminum foil and stored at room temperature for future use.

vi. Preparation of ABMDMA solution:

To prepare a 2.4 mM solution of ABMDMA, 10 mg of AMBDMA (MW= 410.37 g/mol, Sigma Aldrich) was weighed out and placed in a 10 mL volumetric flask. DI water was added to fill approximately half of the flask and the solution was swirled to allow for dissolution. Once the compound was completely dissolved, DI water was added to the mark. The solution was transferred to a capped vial, covered with aluminum foil, and stored at 4 °C.

vii. Measurement of experimentally produced AuNP concentration

The concentration of experimentally produced AuNPs was determined using a Beer-Lambert technique. A commercial, standard solution of AuNPs in citrate with an average diameter of 10 nm (0.05 mg/mL, NanoComposix) was purchased. Solutions with concentrations of 0.05, 0.04, 0.03, 0.02, 0.01, and 0.005 mg/mL were prepared by adding 1,000 µL, 800 µL, 600 µL, 400 µL, 200 µL, and 100 µL of commercial AuNPs to a 1.5 mL microcentrifuge tube. The 2 mM citrate solution was added to result in final volumes of 1 mL. Next, sodium citrate was used as a blank in UV-Vis spectroscopy and the absorbance of each of the standardized solutions at 518 nm was recorded.

A plot of absorbance as a function of concentration was generated to obtain the linear equation of $y = mx + b$. Next, the experimentally generated AuNP solution absorbance was measured at 518 nm. This value was inputted as the y-value into the equation and solved for x which corresponds to the AuNP concentration.

viii. Preparation of LB agar media

To prepare the agar medium, 0.250 L of DI water were added to a 1 L Erlenmeyer flask. Next, 20 g of Luria-Bertani (LB) agar powder (Miller, Difco TM) was weighed out and placed in the 1 L Erlenmeyer flask. An additional 0.250 L of DI water was added to the flask and the solution was mixed with a magnetic stir bar and magnetic stir plate until completely dissolved. Once dissolved, the flask was covered with aluminum foil, secured with autoclave tape, and autoclaved for ~60 minutes (Liquid 15 cycle).

After the autoclave cycle was complete, the flasks were removed from the autoclave using thermal resistant gloves and placed in a bead bath heated to 70 °C (NOTE: The glassware will be hot). While the agar solution is held in the bead bath, single use, sterile petri dishes were spread out in a biological hood. Next the flask containing the agar was removed from the bath and slightly cooled by running room temperature tap water on the outside of the flask for ~30 seconds. The agar solution was then poured into the petri dishes until the solution covered the bottom of the plate. The plates were allowed to cool uncovered in the biological hood for ~15 minutes after which, the lids were placed on each plate, stacked upside down, placed in a plastic sleeve, and stored in the refrigerator for future use. NOTE: Plates must be stored upside down to prevent the accumulation of condensation on the lid

ix. Preparation of LB broth media

To prepare Luria-Bertani broth, 250 mL of DI water was placed in a 1,000 mL Erlenmeyer flask. Next, 10 g of agar powder was weighed out and added to the flask. An additional 250 mL of DI water was added and used to rinse a powder off the sides of the flask. The solution was stirred using a magnetic stir bar and magnetic stir plate until completely dissolved. Once dissolved, the flask is removed from the stir plate, the magnetic stir bar is removed from the flask, and the flask is covered with aluminum foil and secured with autoclave tape. The solution was then autoclaved for ~60 minutes (Liquid15 Cycle). After the cycle is complete, the solution was transferred to a sterilized 1 L bottle and stored at room temperature.

x. Inoculation of *E. Coli*

To generate the liquid *E. Coli* culture, 5 mL of LB broth were measured out in the biological hood using a new, sterile 10 mL glass pipette and an electric pipetman and placed in a

new, sterile 15 mL centrifuge tube. It is important to know that LB Broth is easily contaminated. Therefore, the lid and rim of the LB broth container should be flame sterilized when first opened and before closing to prevent contamination.

Next, the metal inoculating loop was sterilized using cleaner on a paper towel. The loop end was sterilized again by placing it in ethanol and holding it over a Bunsen burner until the ethanol burned off. The loop should be allowed to cool for 15-30 seconds before use. Once the inoculating loop had cooled, the loop end was used to collect a single *E. Coli* colony from the provided stock plate. The loop is directly placed into the centrifuge tube until it touches the LB broth and swirled for 10-15 seconds to release the bacteria colony into the solution.

The 15 mL centrifuge tube was capped, and the inoculating loop was flame sterilized again. The *E. Coli* containing centrifuge tube was placed in the incubator at 37 °C/200 rpm for 18-24 hours. The biological hood and all materials used within it should be sterilized with Amphyl cleaner on a paper towel.

xi. Preparation of new *E. Coli* stock plate

New *E. Coli* stock plates should be grown every 2-4 weeks. To do so, a liquid culture was prepared using the procedure mentioned above. After the incubation period, in a biological hood, a flame sterilized inoculating loop is placed into the liquid culture. The inoculating loop is then streaked onto a new agar plate in the preferred pattern (the quadrant streak pattern is recommended). The plate is then incubated at 37 °C for 18-24 hours. After incubation the plate can be stored in the BSL-1 refrigerator for future use. Again, the biological hood and any materials used in it should be cleaned with Amphyl cleaner on a paper towel.

xii. Bacteria concentration standardization procedure

To standardize the bacteria concentration before the photodeactivation experiment, a liquid culture is prepared as described above. Next, 3.0 mL of the liquid culture is measured into a disposable cuvette and covered with parafilm. The absorbance of the solution at 600 nm was measured (fresh LB broth was used as the blank). The target absorbance is 1.7 OD. If the solution is below the target, the culture must be allowed to incubate for a longer period. However, if the absorbance is higher than the target value, the following dilution calculation can be completed.

Measured Concentration = 2.5

$M = \frac{n}{v}$

$2.5 = \frac{n}{3.00\ mL}$

n = 7.5 mmol

Desired Concentration = 1.7

$M = \frac{n}{v}$

$1.7 = \frac{n}{3.00\ mL}$

n = 5.1 mmol

Volume Needed Replaced w/LB Broth:

7.5 mmol - 5.1 mmol = 2.4 mmol

$2.5 = \frac{2.4\ mmol}{v}$

v = 0.96 mL

xiii. Detailed bacteria irradiation procedure

As discussed in section 2.5, the photodeactivation of bacteria in the presence of various compounds was examined. To do so, a liquid culture was prepared, and the concentration was

standardized as described in procedures ix and xi. After preparation of the bacteria solution, the experimental solutions can be prepared in a six well plate by adding the following volumes depending on the conditions: 100 µL of bacteria, 500 µL of AuNPs, and/or 50 µL of MB. The total volume should be 1,000 µL, therefore any remaining volume after the addition of the bacteria, AuNPs, or MB should be filled with PBS. The experimental solutions can be easily visualized in figure 5 in section 2.5.

After experimental solution preparation, the 6 well plate was covered with aluminum foil and allowed to mix on a shaker plate for 10 minutes at 100 rpm. After the mixing period, the aluminum foil was removed, and the red light was turned on. The plate was irradiated for 5 minutes, while mixing on a shaker plate. A distance of 9 cm from the light source was maintained for each experiment. After irradiation, 100 µL of each experimental solution was placed in a separate 1.5 mL microcentrifuge tube containing 900 uL of PBS to begin serial dilution. After slight mixing with a vortex, 100 µL of the diluted solution was placed in another 1.5 mL microcentrifuge tube containing 900 µL of PBS and vortexed. This process was repeated for a total of 5 microcentrifuge tubes. NOTE: the pipette tip must be changed between each transfer to ensure accurate serial dilution and prevent contamination.

Once the serial dilution was complete, 50 µL from each microcentrifuge tube was carefully spread onto a new petri dish. The metal spreader must be flame sterilized before spreading each plate. The petri dishes were labeled, placed upside-down in an unsealed plastic bag, and allowed to incubate at 37 °C for 18-24 hours. After the incubation period, the plates can be removed and counted.

xiv. Calculation of CFU/mL after irradiation and incubation

To determine the CFU/mL after irradiation, the plates obtained after serial dilution and incubation were counted. To do so, plates with easily identifiable colonies were counted. If the colonies are sperate but there are too many to count, the plate is labeled TNTC ie. too numerous to count. If individual colonies are not visible, the plate is labeled as Lawn. For the plates with countable colonies, a dilution calculation can be done to determine the CFU/mL of the original solution after irradiation.

First, the volume placed on an individual plate was 50 µL out of 1,000. Therefore, the number of colonies should be divided by 0.05 mL. Next, this value can be multiplied by the dilution factor. For example, if the 5th serial dilution plate contained 16 colonies the following calculation would result in the CFU/mL value.

$$\left(\frac{16\ colonies}{0.05\ mL}\right)(100{,}000)\ =\ 3.2\ x\ 10^{7}\ \frac{CFU}{mL}$$

xv. TEM grid preparation

To prepare TEM grids for use, the following procedure was used. Approximately 10-12 Copper grids (SPI, 300 mesh, 3 mm) were washed in hydrochloric acid, DI water, and acetone in sequence. The grids were then placed on filter paper in a petri dish to dry. While the grids dried, a microscope slide (Fisherbrand, Plain precleaned) was soaked in a soap solution for 3-5 minutes. Next, a plastic dispense column was washed with a “wash solution” (ethylene dichloride) and filled to the mark with “Gold solution” (1% formvar in 1,2 dichloroethylene). Once the column was prepared, the microscope slide was removed from the soaking solution and dried using lens paper.

The slide was then carefully placed vertically in the column and allowed to sit for 30-45 seconds. After the time had elapsed, the valve was opened and the “Gold solution” was recollected. Next, the slide was removed from the column and the bottom end placed on a paper towel to collect any additional solution and held for 1-2 minutes to allow the solution to dry onto the slide.

After the solution had dried, the edges of the slide were scratched with a razor 3-5 times. To release the formvar film from the slide, the slide was breathed on and slowly, vertically dipped into a container of DI water. Two thin films separate from the slide until they are completely detached. The TEM grids were then placed bright side down on the gold portion of the thin films. A piece of parafilm was then used to collect the grids by immersing the parafilm directly next to the formvar films at an angle that caused the film to attach to the parafilm. The setup was then placed on a paper towel to dry and stored on filter paper in a petri dish for future use.

To use the TEM grids, a pair of tweezers was used to trace around a single grid. The grid was then held by a pair of tweezers with an o-ring holding it closed. Next, 3 µL of AuNP solution was pipetted onto the grid and allowed to air dry. The grid was then loaded into the TEM for imaging.

xvi. Detailed ROS measurement procedure

To determine the ROS produced in solution, the following procedure was followed. Approximately 800 – 1000 µL of PBS were placed in a 1.5 mL plastic cuvette and used as the blank for the UV-Vis at 400 nm. Next the following volumes were combined in a 1.5 mL plastic cuvette to generate experimental solutions: 100 µL of ABMDMA solution, 500 µL of AuNPs, 50

μL of MB, and/or 200 uL of INF-55 solution. The final solution volume was consistently 1,000 μL. To do so, the remaining volume of filled with PBS. The absorbance for each cuvette was measured at 400 nm for an initial absorbance.

The cuvettes were then covered with parafilm and irradiated for 5 seconds (see figure 6 in section 2.5 for equipment setup). The distance between the light source and the cuvettes was maintained at 9 cm and the solutions were mixed during irradiation on a shaker plate at 100 rpm. After irradiation, the absorbance for each cuvette was measured. The cuvettes were then placed on the shaker plate again and irradiated for 5 more seconds. The absorbance was measured after the second irradiation. This process is repeated until the desired amount of data points have been collected (5, 10, 15, 30, 45, 60, 90, 120, 180, 240, 300, 360, 420, 480, 540, 600 seconds).

APPENDIX C: LASER OPERATIONS

i. Operation of Nanosecond Laser

Before turning on the laser, the “Danger: Laser in Use” sign must be posted outside of the laboratory, those within the lab should be notified, and safety goggles should be put on.

To turn on the laser, the key-switch must be turned 90° counterclockwise to the ON position. The Laser ON light should be illuminated. Next, the laser should be allowed to warm up for 5 minutes. After ~5 minutes, the Q-switch value can be set. To do so, press the SELECT until the Q-SW DELAY LED indicator light is turned on. Using the UP and DOWN buttons, the Q-switch can be set to the desired value (as the Q-switch value increases, the output power value decreases). A Q-switch value of 200 was used for the synthesis procedures.

After setting the Q-switch value, the frequency can be set by pressing the SELECT button until the screen reads F10. The UP and DOWN buttons can be used to adjust the frequency if necessary. A 10 Hz frequency was used for the synthesis procedure. Next, the pulse mode should be checked. To do so, press the SELECT button until the screen reads P00 or P01. If it was set to P00, press the single shot controller button once so that the screen reads P01. Next, press the START/STOP button to turn the laser on. A continuous clicking sound should be audible. The laser should be allowed to run for an additional 5 minutes before opening the shutters. After the 5-minute warm-up period, the first shutter can be opened by pressing the SHUTTER button once. To open the second shutter, the manual slider on the front of the laser must be slid from the closed position to the open position.

If necessary, the Q-switch value can be changed during the laser operation. To do so, both the first and second shutters must be closed. Next, the mode should be changed from P00 to P01 by pressing the UP button. Next, stop the laser by pressing the START/STOP button and change the Q-switch value by pressing SELECT until the Q-switch indicator is lit, and pressing the UP and DOWN buttons to the desired values. The mode can then be changed back to P00 by pressing SELECT until the mode is visible and pressing the single shot controller button once. Once everything has been set, press the START/STOP button to turn the laser back on and open the shutters to resume use.

Once the laser is on, the single shot controller can be used to control the laser operation. By pressing the button once, a single shot will be emitted. By holding the button down, a continuous series of shots will be emitted. This functionality should be used to properly align the laser. To do so, burn paper should be placed in front of each mirror and lens that the laser will interact with, starting with the mirror/lens closest to the laser. Ensure that the burn paper is covered with a single layer of clear tape to prevent dust from accumulating on the optics when aligning the laser. The laser should always be positioned in the center of the mirror or lens to have the desired effect, mitigate interference, and prevent the safety hazard of an uncontrolled beam. Once the laser is aligned, the power should be tested using a power meter before the converging lens. CAUTION: never use the power meter after a converging lens, as a focused laser will damage the meter.

A halfwave plate and polarizer are used to adjust the laser power. As the polarizer divides the beam into a straight path and a perpendicular path, the perpendicular reflection must be

blocked by a beam dump. The straight beam will pass through the halfwave plate and can be rotated clockwise or counterclockwise to control the power.

To turn off the laser, press the START/STOP button. Then, close both the first and second shutters and change the mode from P00 to P01. Wait for 5 minutes and then turn the key switch 90° clockwise to the off position.

ii. Operation of Picosecond Laser

Before turning on the laser, the “Danger: Laser in Use” sign must be posted outside of the laboratory, those within the lab should be notified, and safety goggles should be put on.

To turn on the laser, the power supply for the laser must be plugged in to the outlet. The system should be allowed to sit for 1 minute for the temperature to stabilize. Next, the slave cable should be plugged into the PC. Next, open the Helios Customer GUI (1.0.3.0) shortcut on the desktop and open the HeliosCustomerGui software. When prompted to select the number of COMM-Ports, select 1 and select the COMM-port that corresponds to the slave cable. NOTE: if multiple USBs are plugged into the device, multiple COMM-ports will be visible; however, if the incorrect port is selected, it will result in an error.

Once the interface opens, the desired frequency and pump diode current values can be set according to the values specified on the Laser Test Sheet for the wavelength of choice. Next, close the software, unplug the slave cable, and plug in the master cable. Reselect the number of ports (1 port) and the specific COMM-port being used and enter the appropriate frequency and current values from the Laser Test Sheet. The laser can now be turned on by pressing the START button at the top left corner of the GUI. It takes approximately 10 seconds for the laser to

stabilize after turning it on. To turn off the laser, press the STOP button that appears in place of the START button while the laser is operating.

If the frequency needs to be changed, the laser should be turned off and the previously described steps should be repeated, ie. the software should be closed, the slave settings should be inputted, and the master settings should be inputted. Once operational, the laser beam should be aligned in a similar manner as the nanosecond laser alignment procedure described in the above section. To turn the laser off completely, press the STOP button to stop the beam. Next, close the software, and unplug the power cable.

REFERENCES

(1) Gaynes, R. The Discovery of Penicillin—New Insights After More Than 75 Years of Clinical Use. *Emerg. Infect. Dis.* **2017**, *23* (5), 849–853. https://doi.org/10.3201/eid2305.161556.

(2) *The Nobel Prize in Physiology or Medicine 1945*; Nobel Prize Outreach AB 2024, 2024. https://www.nobelprize.org/prizes/medicine/1945/summary/.

(3) Hutchings, M. I.; Truman, A. W.; Wilkinson, B. Antibiotics: Past, Present and Future. *Curr. Opin. Microbiol.* **2019**, *51*, 72–80. https://doi.org/10.1016/j.mib.2019.10.008.

(4) Fleming-Dutra, K. E.; Hersh, A. L.; Shapiro, D. J.; Bartoces, M.; Enns, E. A.; File, T. M.; Finkelstein, J. A.; Gerber, J. S.; Hyun, D. Y.; Linder, J. A.; Lynfield, R.; Margolis, D. J.; May, L. S.; Merenstein, D.; Metlay, J. P.; Newland, J. G.; Piccirillo, J. F.; Roberts, R. M.; Sanchez, G. V.; Suda, K. J.; Thomas, A.; Woo, T. M.; Zetts, R. M.; Hicks, L. A. Prevalence of Inappropriate Antibiotic Prescriptions Among US Ambulatory Care Visits, 2010-2011. *JAMA* **2016**, *315* (17), 1864. https://doi.org/10.1001/jama.2016.4151.

(5) Hersh, A. L.; King, L. M.; Shapiro, D. J.; Hicks, L. A.; Fleming-Dutra, K. E. Unnecessary Antibiotic Prescribing in US Ambulatory Care Settings, 2010–2015. *Clin. Infect. Dis.* **2020**, ciaa667. https://doi.org/10.1093/cid/ciaa667.

(6) Silver, L. L. Challenges of Antibacterial Discovery. *Clin. Microbiol. Rev.* **2011**, *24* (1), 71–109. https://doi.org/10.1128/CMR.00030-10.

(7) Cižman, M.; Plankar Srovin, T. Antibiotic Consumption and Resistance of Gram-Negative Pathogens (Collateral Damage). *GMS Infect. Dis. 6Doc05* **2018**. https://doi.org/10.3205/ID000040.

(8) Wang, C.-H.; Hsieh, Y.-H.; Powers, Z. M.; Kao, C.-Y. Defeating Antibiotic-Resistant Bacteria: Exploring Alternative Therapies for a Post-Antibiotic Era. *Int. J. Mol. Sci.* **2020**, *21* (3), 1061. https://doi.org/10.3390/ijms21031061.

(9) MacNair, C. R.; Rutherford, S. T.; Tan, M.-W. Alternative Therapeutic Strategies to Treat Antibiotic-Resistant Pathogens. *Nat. Rev. Microbiol.* **2023**. https://doi.org/10.1038/s41579-023-00993-0.

(10) Dai, L.; Sahin, O.; Grover, M.; Zhang, Q. New and Alternative Strategies for the Prevention, Control, and Treatment of Antibiotic-Resistant Campylobacter. *Transl. Res.* **2020**, *223*, 76–88. https://doi.org/10.1016/j.trsl.2020.04.009.

(11) Centers for Disease Control and Prevention (U.S.). *Antibiotic Resistance Threats in the United States, 2019*; Centers for Disease Control and Prevention (U.S.), 2019. https://doi.org/10.15620/cdc:82532.

(12) Centers for Disease Control and Prevention (U.S.). *Antibiotic Resistance Threats in the United States, 2013*; Centers for Disease Control and Prevention (U.S.), 2013. https://stacks.cdc.gov/view/cdc/20705.

(13) Correia, J. H.; Rodrigues, J. A.; Pimenta, S.; Dong, T.; Yang, Z. Photodynamic Therapy Review: Principles, Photosensitizers, Applications, and Future Directions. *Pharmaceutics* **2021**, *13* (9), 1332. https://doi.org/10.3390/pharmaceutics13091332.

(14) Gunaydin, G.; Gedik, M. E.; Ayan, S. Photodynamic Therapy—Current Limitations and Novel Approaches. *Front. Chem.* **2021**, *9*, 691697. https://doi.org/10.3389/fchem.2021.691697.

(15) Kwiatkowski, S.; Knap, B.; Przystupski, D.; Saczko, J.; Kędzierska, E.; Knap-Czop, K.; Kotlińska, J.; Michel, O.; Kotowski, K.; Kulbacka, J. Photodynamic Therapy – Mechanisms, Photosensitizers and Combinations. *Biomed. Pharmacother.* **2018**, *106*, 1098–1107. https://doi.org/10.1016/j.biopha.2018.07.049.
(16) Villalpando-Rodriguez, G. E.; Gibson, S. B. Reactive Oxygen Species (ROS) Regulates Different Types of Cell Death by Acting as a Rheostat. *Oxid. Med. Cell. Longev.* **2021**, *2021*, 1–17. https://doi.org/10.1155/2021/9912436.
(17) Lucky, S. S.; Soo, K. C.; Zhang, Y. Nanoparticles in Photodynamic Therapy. *Chem. Rev.* **2015**, *115* (4), 1990–2042. https://doi.org/10.1021/cr5004198.
(18) Lee, N.-Y.; Ko, W.-C.; Hsueh, P.-R. Nanoparticles in the Treatment of Infections Caused by Multidrug-Resistant Organisms. *Front. Pharmacol.* **2019**, *10*, 1153. https://doi.org/10.3389/fphar.2019.01153.
(19) Perni, S.; Prokopovich, P.; Pratten, J.; Parkin, I. P.; Wilson, M. Nanoparticles: Their Potential Use in Antibacterial Photodynamic Therapy. *Photochem. Photobiol. Sci.* **2011**, *10* (5), 712–720. https://doi.org/10.1039/c0pp00360c.
(20) Zharov, V. P.; Mercer, K. E.; Galitovskaya, E. N.; Smeltzer, M. S. Photothermal Nanotherapeutics and Nanodiagnostics for Selective Killing of Bacteria Targeted with Gold Nanoparticles. *Biophys. J.* **2006**, *90* (2), 619–627. https://doi.org/10.1529/biophysj.105.061895.
(21) Gao, W.; Zhang, L. Nanomaterials Arising amid Antibiotic Resistance. *Nat. Rev. Microbiol.* **2021**, *19* (1), 5–6. https://doi.org/10.1038/s41579-020-00469-5.
(22) Makabenta, J. M. V.; Nabawy, A.; Li, C.-H.; Schmidt-Malan, S.; Patel, R.; Rotello, V. M. Nanomaterial-Based Therapeutics for Antibiotic-Resistant Bacterial Infections. *Nat. Rev. Microbiol.* **2021**, *19* (1), 23–36. https://doi.org/10.1038/s41579-020-0420-1.
(23) Gupta, A.; Mumtaz, S.; Li, C.-H.; Hussain, I.; Rotello, V. M. Combatting Antibiotic-Resistant Bacteria Using Nanomaterials. *Chem. Soc. Rev.* **2019**, *48* (2), 415–427. https://doi.org/10.1039/C7CS00748E.
(24) Kidron, A.; Nguyen, H. *Phenothiazine*; StatePearls, 2023.
(25) Oz, M.; Lorke, D. E.; Hasan, M.; Petroianu, G. A. Cellular and Molecular Actions of Methylene Blue in the Nervous System. *Med. Res. Rev.* **2011**, *31* (1), 93–117. https://doi.org/10.1002/med.20177.
(26) Boltes Cecatto, R.; Siqueira De Magalhães, L.; Fernanda Setúbal Destro Rodrigues, M.; Pavani, C.; Lino-dos-Santos-Franco, A.; Teixeira Gomes, M.; Fátima Teixeira Silva, D. Methylene Blue Mediated Antimicrobial Photodynamic Therapy in Clinical Human Studies: The State of the Art. *Photodiagnosis Photodyn. Ther.* **2020**, *31*, 101828. https://doi.org/10.1016/j.pdpdt.2020.101828.
(27) Chan, H.; Pavelka, M. S.; Baran, T. M. Methylene Blue Photodynamic Therapy of Bacterial Species Found in Human Abscesses: Planktonic, Biofilm, and 3D Silicone Models. *Proc. SPIE-- Int. Soc. Opt. Eng.* **2023**, *12358*, 1235805.
(28) Zada, L.; Anwar, S.; Imtiaz, S.; Saleem, M.; Shah, A. A. In Vitro Study: Methylene Blue-Based Antibacterial Photodynamic Inactivation of Pseudomonas Aeruginosa. *Appl. Microbiol. Biotechnol.* **2024**, *108* (1), 169. https://doi.org/10.1007/s00253-024-13009-5.
(29) Dykman, L. A.; Khlebtsov, N. G. Gold Nanoparticles in Biology and Medicine: Recent Advances and Prospects. *Acta Naturae* **2011**, *3* (2), 34–55.

(30) Bucharskaya, A.; Maslyakova, G.; Terentyuk, G.; Yakunin, A.; Avetisyan, Y.; Bibikova, O.; Tuchina, E.; Khlebtsov, B.; Khlebtsov, N.; Tuchin, V. Towards Effective Photothermal/Photodynamic Treatment Using Plasmonic Gold Nanoparticles. *Int. J. Mol. Sci.* **2016**, *17* (8), 1295. https://doi.org/10.3390/ijms17081295.
(31) Gamaleia, N. F.; Shton, I. O. Gold Mining for PDT: Great Expectations from Tiny Nanoparticles. *Photodiagnosis Photodyn. Ther.* **2015**, *12* (2), 221–231. https://doi.org/10.1016/j.pdpdt.2015.03.002.
(32) García Calavia, P.; Bruce, G.; Pérez-García, L.; Russell, D. A. Photosensitiser-Gold Nanoparticle Conjugates for Photodynamic Therapy of Cancer. *Photochem. Photobiol. Sci.* **2018**, *17* (11), 1534–1552. https://doi.org/10.1039/C8PP00271A.
(33) Maliszewska, I.; Wanarska, E.; Thompson, A. C.; Samuel, I. D. W.; Matczyszyn, K. Biogenic Gold Nanoparticles Decrease Methylene Blue Photobleaching and Enhance Antimicrobial Photodynamic Therapy. *Molecules* **2021**, *26* (3), 623. https://doi.org/10.3390/molecules26030623.
(34) Okkeh, M.; Bloise, N.; Restivo, E.; De Vita, L.; Pallavicini, P.; Visai, L. Gold Nanoparticles: Can They Be the Next Magic Bullet for Multidrug-Resistant Bacteria? *Nanomaterials* **2021**, *11* (2), 312. https://doi.org/10.3390/nano11020312.
(35) Sherwani, Mohd. A.; Tufail, S.; Khan, A. A.; Owais, M. Gold Nanoparticle-Photosensitizer Conjugate Based Photodynamic Inactivation of Biofilm Producing Cells: Potential for Treatment of C. Albicans Infection in BALB/c Mice. *PLOS ONE* **2015**, *10* (7), e0131684. https://doi.org/10.1371/journal.pone.0131684.
(36) Pissuwan, D.; Cortie, C. H.; Valenzuela, S. M.; Cortie, M. B. Functionalised Gold Nanoparticles for Controlling Pathogenic Bacteria. *Trends Biotechnol.* **2010**, *28* (4), 207–213. https://doi.org/10.1016/j.tibtech.2009.12.004.
(37) Shukla, R.; Bansal, V.; Chaudhary, M.; Basu, A.; Bhonde, R. R.; Sastry, M. Biocompatibility of Gold Nanoparticles and Their Endocytotic Fate Inside the Cellular Compartment: A Microscopic Overview. *Langmuir* **2005**, *21* (23), 10644–10654. https://doi.org/10.1021/la0513712.
(38) Herizchi, R.; Abbasi, E.; Milani, M.; Akbarzadeh, A. Current Methods for Synthesis of Gold Nanoparticles. *Artif. Cells Nanomedicine Biotechnol.* **2016**, *44* (2), 596–602. https://doi.org/10.3109/21691401.2014.971807.
(39) Mat Isa, S. Z.; Zainon, R.; Tamal, M. State of the Art in Gold Nanoparticle Synthesisation via Pulsed Laser Ablation in Liquid and Its Characterisation for Molecular Imaging: A Review. *Materials* **2022**, *15* (3), 875. https://doi.org/10.3390/ma15030875.
(40) Ielo, I.; Rando, G.; Giacobello, F.; Sfameni, S.; Castellano, A.; Galletta, M.; Drommi, D.; Rosace, G.; Plutino, M. R. Synthesis, Chemical–Physical Characterization, and Biomedical Applications of Functional Gold Nanoparticles: A Review. *Molecules* **2021**, *26* (19), 5823. https://doi.org/10.3390/molecules26195823.
(41) Kim, H.; Lee, D. Near-Infrared-Responsive Cancer Photothermal and Photodynamic Therapy Using Gold Nanoparticles. *Polymers* **2018**, *10* (9), 961. https://doi.org/10.3390/polym10090961.
(42) Balachandran, A.; Sreenilayam, S. P.; Madanan, K.; Thomas, S.; Brabazon, D. Nanoparticle Production via Laser Ablation Synthesis in Solution Method and Printed Electronic Application - A Brief Review. *Results Eng.* **2022**, *16*, 100646. https://doi.org/10.1016/j.rineng.2022.100646.

(43) Park, J.-W.; Shumaker-Parry, J. S. Structural Study of Citrate Layers on Gold Nanoparticles: Role of Intermolecular Interactions in Stabilizing Nanoparticles. *J. Am. Chem. Soc.* **2014**, *136* (5), 1907–1921. https://doi.org/10.1021/ja4097384.
(44) Ma, C.; Gerhard, E.; Lu, D.; Yang, J. Citrate Chemistry and Biology for Biomaterials Design. *Biomaterials* **2018**, *178*, 383–400. https://doi.org/10.1016/j.biomaterials.2018.05.003.
(45) Grys, D.-B.; De Nijs, B.; Salmon, A. R.; Huang, J.; Wang, W.; Chen, W.-H.; Scherman, O. A.; Baumberg, J. J. Citrate Coordination and Bridging of Gold Nanoparticles: The Role of Gold Adatoms in AuNP Aging. *ACS Nano* **2020**, *14* (7), 8689–8696. https://doi.org/10.1021/acsnano.0c03050.
(46) Blair, J. M. A.; Webber, M. A.; Baylay, A. J.; Ogbolu, D. O.; Piddock, L. J. V. Molecular Mechanisms of Antibiotic Resistance. *Nat. Rev. Microbiol.* **2015**, *13* (1), 42–51. https://doi.org/10.1038/nrmicro3380.
(47) Webber, M. A. The Importance of Efflux Pumps in Bacterial Antibiotic Resistance. *J. Antimicrob. Chemother.* **2003**, *51* (1), 9–11. https://doi.org/10.1093/jac/dkg050.
(48) Sharma, A.; Gupta, V.; Pathania, R. Efflux Pump Inhibitors for Bacterial Pathogens: From Bench to Bedside. *Indian J. Med. Res.* **2019**, *149* (2), 129. https://doi.org/10.4103/ijmr.IJMR_2079_17.
(49) Alenazy, R. Drug Efflux Pump Inhibitors: A Promising Approach to Counter Multidrug Resistance in Gram-Negative Pathogens by Targeting AcrB Protein from AcrAB-TolC Multidrug Efflux Pump from Escherichia Coli. *Biology* **2022**, *11* (9), 1328. https://doi.org/10.3390/biology11091328.
(50) Smith, B. L.; Fernando, S.; King, M. D. Escherichia Coli Resistance Mechanism AcrAB-TolC Efflux Pump Interactions with Commonly Used Antibiotics: A Molecular Dynamics Study. *Sci. Rep.* **2024**, *14* (1), 2742. https://doi.org/10.1038/s41598-024-52536-z.
(51) Jang, S. AcrAB-TolC, a Major Efflux Pump in Gram Negative Bacteria: Toward Understanding Its Operation Mechanism. *BMB Rep.* **2023**, *56* (6), 326–334. https://doi.org/10.5483/BMBRep.2023-0070.
(52) Du, D.; Wang, Z.; James, N. R.; Voss, J. E.; Klimont, E.; Ohene-Agyei, T.; Venter, H.; Chiu, W.; Luisi, B. F. Structure of the AcrAB–TolC Multidrug Efflux Pump. *Nature* **2014**, *509* (7501), 512–515. https://doi.org/10.1038/nature13205.
(53) Husain, F.; Nikaido, H. Substrate Path in the AcrB Multidrug Efflux Pump of Escherichia Coli: Substrate Path in AcrB. *Mol. Microbiol.* **2010**, *78* (2), 320–330. https://doi.org/10.1111/j.1365-2958.2010.07330.x.
(54) Pos, K. M. Drug Transport Mechanism of the AcrB Efflux Pump. *Biochim. Biophys. Acta BBA - Proteins Proteomics* **2009**, *1794* (5), 782–793. https://doi.org/10.1016/j.bbapap.2008.12.015.
(55) Takatsuka, Y.; Chen, C.; Nikaido, H. Mechanism of Recognition of Compounds of Diverse Structures by the Multidrug Efflux Pump AcrB of *Escherichia Coli*. *Proc. Natl. Acad. Sci.* **2010**, *107* (15), 6559–6565. https://doi.org/10.1073/pnas.1001460107.
(56) Shaheen, A.; Afridi, W. A.; Mahboob, S.; Sana, M.; Zeeshan, N.; Ismat, F.; Mirza, O.; Iqbal, M.; Rahman, M. Reserpine Is the New Addition into the Repertoire of AcrB Efflux Pump Inhibitors. *Mol. Biol.* **2019**, *53* (4), 596–605. https://doi.org/10.1134/S0026893319040113.

(57) Kimling, J.; Maier, M.; Okenve, B.; Kotaidis, V.; Ballot, H.; Plech, A. Turkevich Method for Gold Nanoparticle Synthesis Revisited. *J. Phys. Chem. B* **2006**, *110* (32), 15700–15707. https://doi.org/10.1021/jp061667w.
(58) Dinga, D. K.; Bredol, M.; Kynast, U. Novel Approach toward Water-Soluble Singlet Oxygen Monitors Based on Hybrid Inorganic–Organic Nanoclay. *J. Phys. Chem. C* **2021**, *125* (39), 21496–21502. https://doi.org/10.1021/acs.jpcc.1c04785.
(59) Entradas, T.; Waldron, S.; Volk, M. The Detection Sensitivity of Commonly Used Singlet Oxygen Probes in Aqueous Environments. *J. Photochem. Photobiol. B* **2020**, *204*, 111787. https://doi.org/10.1016/j.jphotobiol.2020.111787.
(60) Verbruggen, S. W.; Keulemans, M.; Martens, J. A.; Lenaerts, S. Predicting the Surface Plasmon Resonance Wavelength of Gold–Silver Alloy Nanoparticles. *J. Phys. Chem. C* **2013**, *117* (37), 19142–19145. https://doi.org/10.1021/jp4070856.
(61) Drummen, G.; Zamiri; Zakaria; Ahangar; Darroudi, M.; Zamiri; Rizwan. The Effect of Laser Repetition Rate on the LASiS Synthesis of Biocompatible Silver Nanoparticles in Aqueous Starch Solution. *Int. J. Nanomedicine* **2013**, 233. https://doi.org/10.2147/IJN.S36036.
(62) Abdelhalim, M. A. K.; M. Mady, M. Physical Properties of Different Gold Nanoparticles: Ultraviolet-Visible and Fluorescence Measurements. *J. Nanomedicine Nanotechnol.* **2012**, *03* (03). https://doi.org/10.4172/2157-7439.1000133.
(63) Zheng, J.; Zhou, C.; Yu, M.; Liu, J. Different Sized Luminescent Gold Nanoparticles. *Nanoscale* **2012**, *4* (14), 4073. https://doi.org/10.1039/c2nr31192e.
(64) Ishida, T.; Murayama, T.; Taketoshi, A.; Haruta, M. Importance of Size and Contact Structure of Gold Nanoparticles for the Genesis of Unique Catalytic Processes. *Chem. Rev.* **2020**, *120* (2), 464–525. https://doi.org/10.1021/acs.chemrev.9b00551.
(65) Yeh, Y.-C.; Creran, B.; Rotello, V. M. Gold Nanoparticles: Preparation, Properties, and Applications in Bionanotechnology. *Nanoscale* **2012**, *4* (6), 1871–1880. https://doi.org/10.1039/C1NR11188D.
(66) De Jong, W. H.; Hagens, W. I.; Krystek, P.; Burger, M. C.; Sips, A. J. A. M.; Geertsma, R. E. Particle Size-Dependent Organ Distribution of Gold Nanoparticles after Intravenous Administration. *Biomaterials* **2008**, *29* (12), 1912–1919. https://doi.org/10.1016/j.biomaterials.2007.12.037.
(67) Tam, H.-K.; Foong, W. E.; Oswald, C.; Herrmann, A.; Zeng, H.; Pos, K. M. Allosteric Drug Transport Mechanism of Multidrug Transporter AcrB. *Nat. Commun.* **2021**, *12* (1), 3889. https://doi.org/10.1038/s41467-021-24151-3.
(68) Zwama, M.; Yamasaki, S.; Nakashima, R.; Sakurai, K.; Nishino, K.; Yamaguchi, A. Multiple Entry Pathways within the Efflux Transporter AcrB Contribute to Multidrug Recognition. *Nat. Commun.* **2018**, *9* (1), 124. https://doi.org/10.1038/s41467-017-02493-1.
(69) Trampari, E.; Prischi, F.; Vargiu, A. V.; Abi-Assaf, J.; Bavro, V. N.; Webber, M. A. Functionally Distinct Mutations within AcrB Underpin Antibiotic Resistance in Different Lifestyles. *Npj Antimicrob. Resist.* **2023**, *1* (1), 2. https://doi.org/10.1038/s44259-023-00001-8.
(70) Blair, J. M. A.; Bavro, V. N.; Ricci, V.; Modi, N.; Cacciotto, P.; Kleinekathöfer, U.; Ruggerone, P.; Vargiu, A. V.; Baylay, A. J.; Smith, H. E.; Brandon, Y.; Galloway, D.; Piddock, L. J. V. AcrB Drug-Binding Pocket Substitution Confers Clinically Relevant

Resistance and Altered Substrate Specificity. *Proc. Natl. Acad. Sci.* **2015**, *112* (11), 3511–3516. https://doi.org/10.1073/pnas.1419939112.

Copyright Permission

Name: ben Yosef, Justice

Email (to receive future readership statistics): justice.benyosef471@topper.wku.edu

Type of document: ['Thesis']

Title: Synthesis of Gold Nanoparticles via Pulsed Liquid Ablation for use in the Photodynamic Therapy of Bacteria

Keywords (3-5 keywords not included in the title that uniquely describe content): Efflux Pump Inhibitor, Metal Nanoparticles, Laser Ablation, Antibiotic Resistant Bacteria

Committee Chair: Dr. Ali Oguz Er

Additional Committee Members: Dr. Lawrence Hill
Dr. Matthew Nee

Select 3-5 TopSCHOLAR® disciplines for indexing your research topic in TopSCHOLAR®: Life Sciences, Medicine and Health Sciences, Physical Sciences and Mathematics

access.']

The person whose information is entered above grants their consent to the collection and use of their information consistent with the Privacy Policy. They acknowledge that the use of this service is subject to the Terms and Conditions.

['I consent to the above statement.']